

ISSN 0377-9416



www.pmai.in

TRANSACTIONS OF POWDER METALLURGY ASSOCIATION OF INDIA

Vol. 46 No.1 & 2, June-December 2020

Chief Editor - P. Ramakrishnan

ISSN 0377-9416



www.pmai.in

TRANSACTIONS OF POWDER METALLURGY ASSOCIATION OF INDIA

Vol. 46 No.1 & 2, June - December 2020

Chief Editor - P. Ramakrishnan



Powder Metallurgy Association of India

Office Bearers

President

Shri Aniket Gore

Vice President

Shri Deepak Grover
Shri Narendra Dhokey
Shri Rajendra Sethiya
Shri Siddharth Singhal

General Secretary

Dr. Deep Prakash

Hon. Treasurer

Dr. Murli Gopal Krishnamoorty

Joint Secretary

Shri Amit Sinha
Shri Malobika Karanjai



Chief Editor

Prof. Ramakrishnan P.

Editorial Advisory Board

Dr. Ashok S.

Mr. Chandrachud N.L.

Dr. Rama Mohan T. R.

Editorial Board

Dr. Appa Rao G.

Dr. Bhargava Parag

Dr. Dabhade Vikram

Dr. Deep Prakash

Dr. Dhokey N.B.

Dr. Kumar Y.V.S.

Dr. Malobika Karanjai

Dr. Murli Gopal K.

Dr. Panigrahi B.B.

Dr. Sastry I.S.R.

Dr. Tarasankar Mahata

Published by :

**Powder Metallurgy Association
of India (PMAI)**

102, Anandi, 1st Floor,

M.B. Raut Road, Shivaji Park,

Dadar, Mumbai - 400028, India

Tel.: +91 9820951180

+91 9821111677

E-mail: info@pmai.in

Neither the Powder Metallurgy Association of India nor the editor assumes responsibility of opinions expressed by the authors of the papers published in this transaction.

Editorial



International Conference & Exhibition PM 20, along with the 46th. ATM was organized during Feb.19-21, 2020 at The Lalit Mumbai. Trans. PMAI, Vol.46,2020 contain selected papers from this successful event. The rampaging waves of COVID 19 has transformed our lives and affected the publication of this volume of Transaction.

The first paper reviews the various powder mixes the powder metal parts maker can choose, particularly when the parts become more complicated. These include premixes, dust free mixes, mixes for warm die compaction and cost effective organic binder mixes. This is followed by an article on material options for high temperature sintering provide alternate alloying elements incorporating Cr, Si and V which will address issues like price, environmental and recyclability concern. Next is the PM-20 award winning paper; improvement of mechanical properties of AlCoCrNiSi high entropy alloy by Ni additive sintering. The overall processing consists of preparation of light weight alloy powders by mechanical alloying followed by nickel additions and hot pressing. This is followed by a paper dealing with a family of high strength and cost effective PM steels developed by mixing selected combinations of alloying elements such as Cr, Ni and Cu in different and predetermined concentrations.

Next paper is dealing with the AlCoNiWc high entropy alloy coating on carbon steel, which has provided a high wear and corrosion resistance at high temperatures. The design and development of environment friendly β -Zn4Sb3 for the proposed application in the thermoelectric coolers is the subject matter of the next PM20 award winning paper. This is followed by an article on the commercial use of SMC in electrical buses, resulted in overall lower production cost along with additional benefit of improved motor performance. Another award winning paper is suggesting that small addition of Ca doping is favorable for enhancing the electrochemical properties of $\text{Nd}_2\text{NiO}_{4+\delta}$ for solid oxide fuel cell applications. The concluding paper is on the synthesis and characterization of Lithium cerate ceramics for breeder application for fusion energy which has a great potential in the future.

P. Ramakrishnan

TRANSACTIONS OF
POWDER METALLURGY ASSOCIATION OF INDIA

Vol. 46 No.1 &2, June-December 2020

CONTENTS

1 Premixes, Clean Mixes, Lean Alloys and Engineered Mixes <i>S R Sundaram</i>	1-6
2 Material Options for High Temperature Sintering <i>Kylan McQuaig, Neal Kraus, Bruce Lindsley</i>	7-12
3 Improvement of Mechanical Properties of AlCoCrFeNiSi High Entropy Alloy by Ni Additive Sintering <i>Sahil Rohila, Subhendu Naskar, Bharat B. Panigrahi</i>	13-20
4 Sintering Conditions and Mechanical Performances of Low Nickel PM Chromium Steels <i>Ivan Lorenzon, Franco Buzzelli, Mirko Nassuato</i>	21-26
5 Microstructural Characterization of AlCoNiVWC High Entropy Alloy Cladding on IS2062 Steel <i>A. Verma, M. Abhinav, Shanmugasundaram T.</i>	27-32
6 Wear and Friction Behavior of NiCrBSi Coatings at Elevated Temperature <i>Nikita Mohite, Crystal Liu, Hans Hallen, Bruc Zhang, Kari Westerling, Mangesh Patil, Amitava Sen</i>	33-36
7 Design and Development of Environment Friendly Material for Thermoelectric Coolers <i>Natasha Nayak, Harshavardhan Patil and N. B. Dhokey</i>	37-40
8 Commercial Use of SMC in Electrical Buses <i>R. Guo, M. Nie, S. Grenier, D. Tremblay</i>	41-42
9 Preparation and Electrochemical Characterization of Ca Doped Nd₂NiO_{4+δ} Solid Oxide Fuel Cell Cathode Material <i>Pranjal Gandhre, R K Lenka, P K Patro, L. Muhmood, and T Mahata</i>	43-49
10 Synthesis and Characterisation of Lithium Cerate Ceramics for Breeder Application <i>Nida Khan, Amit Sinha, S. R. Nair, R.K. Lenka and V. Sudarsan</i>	50-55

PREMIXES, CLEAN MIXES, LEAN ALLOYS AND ENGINEERED MIXES

S R Sundaram

FPMAL, Bangalore, India

Abstract: *Status of Technology: Globally automotive forms the largest as also the fastest growing, application for Powder Metallurgy which is stated to compound annually to 6.5% over 2017-2023 reaching a projected 7.8 Billion Dollars. [1] The overall Powder metallurgy market is estimated to reach this figure of 7.8 Billion Dollars in 2018. One major factor for choosing PM, is energy efficiency and conservation of RM to the extent of 95% of input Raw Material. The 3 D printing technologies pose some problems due to high Capex and use of very high Raw Material Prices. Several Powder Metallurgy Technologists are working on further better use of Raw Material to the extent of 98-99% and cutting Raw Material costs. Premixes, Clean mixes, Lean alloys, Engineered Solutions with special lubricants: A lot of detailed work has been done and Component specific mixes with have been used. This paper reviews the various types of features with are currently available in Powder mixes which the Powder Metal parts maker can choose from.*

Introduction

In a country like India, with collaborations with many countries, and the due to the need to follow the collaborators' specifications, there were a plethora of compositions and all these were of small volume. So it was necessary for the parts manufacturer to do in-plant mixing. A parts manufacturer had a large mix list up to 200 compositions, often varying only in the Carbon/Copper content.

World over the situation was same. Over a period of time Global business volumes grew and also standardization of chemistry by OEMS meant larger volumes as also with less chemistry variations.

The Genre of Premixes was born.

The parts makers could order a mix of a particular chemistry which would be delivered by the powder producer. The volumes were high enough for the Premix to compete economically with in-plant mixes. This also reduced problems of the parts producer to carry expensive inventory of ingredients in the various mixes as also the need to invest mixing equipment / develop mixing skills.

It necessitated powder producers who hitherto delivered Pure Metal powders to learn to produce Premixes with specific Green properties and Strengths and Sintered properties and strengths as needed by the parts producers. Often it led to a collaborative effort between Powder and Part producer to achieve a proper Premix.

Although premixes are used in Ferrous and Non-ferrous compositions, by the sheer preponderance of volumes of Ferrous Sintered Parts this paper reviews the Ferrous Premixes only.

Premixes

A normal premix is just a mechanical mixture of the ingredients. The early examples were PASC, and SNC powders Höganäs (Sweden). Although these had specific names, these were essentially premixes of Phosphorous and Sulphur and they sell in large volumes. Present day premixes may contain 5 to 6 ingredients,

Many types of Premixes suffered from problems of In-Plant mixes in that there was segregation of Carbon (added as Graphite) if the mix contained more than 0.5% by weight. This was due to large difference in bulk densities between graphite

and the metallic additions. It was necessary to overcome this problem.

Bonded mixes (also called “Clean Mixes”)

The basic principle is to use an Organic Binder dissolved in a solvent to coat all mix ingredients, which upon drying, sticks to Iron powder. Fig 1. There are patents of Hoeganaes which are nearly 20 years old. This method however has gained currency now, and almost all manufacturers offer some bonded mix using proprietary Binder. There are different brand names from “Starmix” of Höganäs, “Flomet” of Rio Tinto, Clean Mix of JFE metal powders (Earlier Kawasaki).^[2]

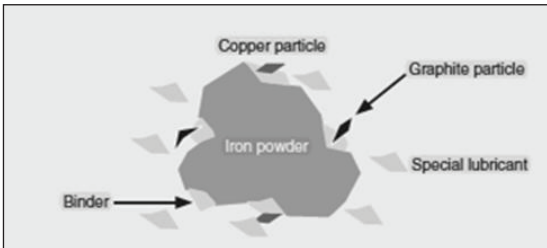


Fig. 1 Design of a Bonded mix Design of a Bonded mix

Whatever name by which you call Bonded Mixes they all have similar advantages :

1. Faster flow (Helps filling the difficult to reach the parts of die)
2. Reduces segregation of ingredients (Carbon chiefly).
3. Ensures there is practically Dust-Free when transferring blender to container, and from Bag to Press, and while compaction (This is why one manufacturer calls it “Clean Mix”)^[2]

A similar binder Technique can be used when hybrid materials are used, in place of Pure Iron powder, for e.g. Molybdenum is prealloyed while making the alloy powder and all other ingredients like Ni, Cu, C are treated to this powder with binder. Fig 2.

It has become a standard practice to add Molybdenum while making the Iron powder as the diffusion rates are very poor when Molybdenum is added as elemental addition to Iron powder.

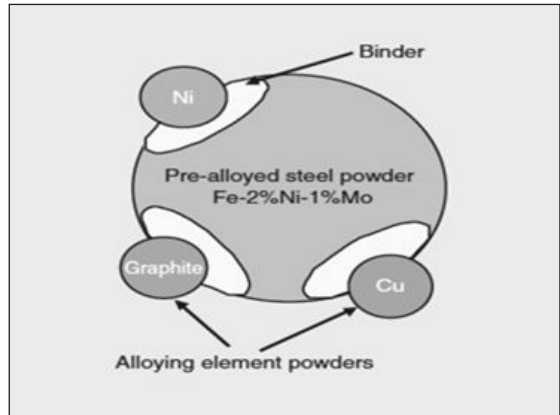


Fig. 2 Design of a Hybrid bonded mix

Lean alloys

It is known that Pre-Alloyed powders sacrifice Compressibility, and are expensive although they are otherwise convenient. Höganäs of Sweden came with a solution to both the problems- Compressibility and Cost. They introduced a series of powders named “Distalloys”. Distalloy is term they used for Diffusion Alloying, where a mechanical mix of various elements is thermally treated and leads to the elements partially alloyed to the Iron powder but mostly in elemental form protecting compressibility.

There a series of Ni-Cu-Mo Distalloys to choose from, the total alloy content in these Distalloys of Höganäs, varied from 3.75% to 6.0%. They introduced a lean alloy Distalloy AQ contained just 0.5% Ni and 0.5% Mo i.e. a total of 1%.^[3] However still usual Distalloys with 4-6% alloy contents are favorites of parts makers. Other manufacturers have their equivalent of the Höganäs Distalloys.

Development of highly compressible leaner alloyed steel powders equivalent to Mo-Ni-Cu is reported by Rio Tinto Metal powders, Canada. This work was considered important as the increase in price of Ni, and Mo. Much work has been done by powder producers, reported in various conferences focused on use of Cr, Mn, or Si.

Organic Bonding as against Diffusion bonded alloys

Two different studies were reported by Rio Tinto that were aimed at developing leaner Mo-Ni-Cu powders as cost effective replacements for the commonly used diffusion alloyed grades FD-0405 (0.5 Mo-4Ni-1.5 Cu) and FD-0205 (0.5 Mo-1.75 Ni-1.5 Cu). The basis for this case study was the replacement of FD-0405 the use of “organic bonding” to bind Ni and Cu additions to pre alloyed Mo steel grades [4].

The term “Organic Bonding” was used to describe the use of binder treatment of Ni and Cu only with graphite and lubricant addition being conventional admixing as opposed to a “conventional binder treatment” where all four additions are binder treated. The choice was based on data in Table 1. and the cost benefits in respect of sintered properties is shown in Table 2.

Table 1. Description of Mixes.(Taguchi) All mixes contained 0.6% EBS wax as lubricant. [4]

Mix #	Pre-Alloyed Mo%	Admixed Ni%	Admixed Cu%	Graphite %	Cost Index
1	0.0 (1001)	2.5	1.0	1.0	0.67
2	0.5(4001)	2.5	1.25	1.25	0.77
3	0.85(4401)	2.5	1.5	1.5	0.84
4	0.5(4001)	3.0	1.5	1.5	0.85
5	0.85(4401)	3.0	1.0	1.0	0.88
6	0.0 (1001)	3.0	1.25	1.25	0.76
7	0.85(4401)	3.5	1.25	1.25	0.96
8	0.0(1001)	3.5	1.5	1.5	0.84
9	0.5(4001)	3.5	1.0	1.0	0.89
AVG	0.5	3.0	1.25	1.25	0.83
REF	1.25	4.0	1.0	1.5	1.0

Table 2. Cost benefit of Lean organic bonded powder compared with FD-0405 diffusion alloyed powder. (Compaction 540Mpa; Standard Sintering conditions). M Measured; E* Estimated. [4]*

Mix ID	Process	Chemistry	Cost Index	AD, g/cm ³	Flow, s/50g	S. Dens, g/cm ³	TRS, MPa	Hard. HRA (HRC)	DC vs green, %	UTS, MPa	YS, MPa	Elong. %	
Ref	Diff-Alloyed	0.5Mo-4Ni-1.5Cu-0.6C	1.0	3.10	37	M*	6.99	59.0 [18.2]	-0.22	725	517	1.1	
						E*	6.98	1626	58.4 [17.1]	-0.21	788	520	2.2
F48 Lean	Org.-bonded	0.85Mo-2.3Ni-1.15Cu-0.6C	0.80	3.04	32	M*	7.05	1600	59.0 [18.2]	-0.20	757	659	0.5
						E*	7.03	1622	59.6 [19.3]	-0.22	906	636	1.3

The authors concluded :

- 1) Adding elemental Ni is not a Cost effective way to increase sintered properties.

- 2) Increasing Mo level is highly beneficial for static strength (TRS,UTS, and YS). On the other hand it has almost no effect on hardness.

Overall, even if costly, Mo allows increasing sintered properties in a cost effective way.[4]

Lubricants and Engineered Mixes

The Lubricant just called Lube in the ingredients in the Premix and added 0.6% -0.8%, but plays a large role in the properties of the premix. Generally we tend to use EBS (Ethylene Bis Stearamide) wax or Zinc Stearate as a lubricant and believe it is all done. But there are lots of factors in the Lubricant which will change the way a Premix behaves.

The ideal lubricant allows for good flow and packing, facilitates low ejection stresses while creating a compact with good green strength, exits the part entirely during sintering and provides a good surface finish. Lubricant burn-out is an important step and choice of lubricant with ineffective burn off, can cause visible stains or soot to accumulate on the surface of the part.

Commercially available lubricants are EBS Wax in powder form, Acrawax (Atomised as fine powder), Zinc Stearate and a chemically processed proprietary lubricant named Kenolube by Höganäs (available to customers who buy Höganäs powders).

If you look at particle size and Zinc content of various Lubricants:

The principal benefits of Zinc Stearate are, good powder properties, with fast flow and high apparent density. High green and sintered density is obtained with small pores. Its disadvantages are high ejection energy and Zinc content, which may cause staining of the component and Zinc accumulation in furnace. Mixes with metal stearates also form more dust than mixes with other lubricants.

Amide wax has the advantage of small pores compared to other lubricants due to small particle size. Since Amide wax is purely organic it has very good burn off properties. The apparent density is low and powder flow is poorer than other lubricants.

Kenolube combines the good powder properties of Zinc Stearate with the lubrication that it surpasses Amide wax. Green strength obtained with Kenolube is higher compared with Zinc Stearate and Amide Wax.

Metallub has the advantages of very good lubrication, higher apparent density, and good flow on the other hand it has low green and sintered density, and the component has large pores as shown in Fig.3 & Table 3.

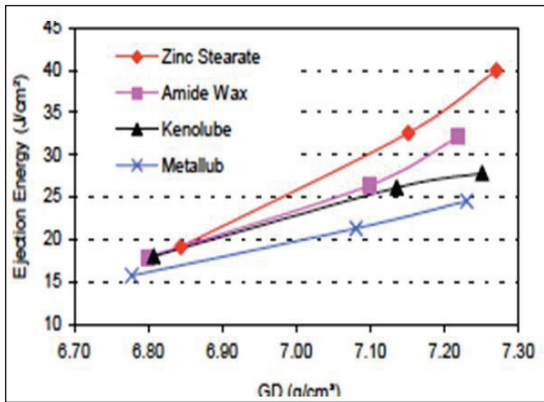


Fig. 3. Ejection Energy Vs Green Density of mix with Distaloy AE +0.5C + Lubricant. [5]

Table 3. Particle Size and Zinc Content [5]

	Zinc Stearate	Amide Wax	Metallub	Keno lube
D50	4µm	7µm	45µm	20µm
Zn	11%	---	10%	2%

You choose a lubricant depending on what you want.

Engineered Mixes for Warm Die Compaction

If a part with very high density (~7.35 gm / cc) is considered to be made, you will need warm die compaction. Then the die temperature will

be in the range of 63- 105°Celsius. The lubricant used must retain lubricity, as well as low ejection force at these temperatures. It must have good burn out characteristics during sintering. The lubricant must not have a large liquid component at these enhanced temperatures that may cause loose powder to stick to tool elements which may cause tool damage and may lead to poor quality of surface of the part.

The final performance aspect of this lubricant is its ability to perform at higher compaction pressures to get the requisite high densities. Thus the lubricant must perform well at compaction pressures ranging from 690 to 827 Mpa, and still be able to flow to the die wall for maximum lubrication as shown in Table 4.

Table 4. Green and Ejection Properties of FLN2-4405 Mix. [6]

Lubricant	Compacted 827 MPa	Green Density (g/cm³)	Green Strength (MPa)	Strip (MPa)	Slide (MPa)
	Compaction Temperature				
Acrax C (0.75%)	25°C	7.19	18	21	17
AncorLube (0.40%)	60°C	7.34	23	18	17
AncorLube (0.40%)	77°C	7.36	25	18	17
AncorLube (0.40%)	107°C	7.38	25	17	17

Various powder manufacturers offer premixes with their own Proprietary brand of Special lubricants for Warm die compaction.

Höganäs' INTRA LUBE-E and INTRA LUBE HD; Hoeganaes' ANCOR LUBE and ANCOR MAX Series: Rio Tinto's HD A, HD C and HD W; JFE Steels' JIP Clean mix HDX, and JDX-CMX are some of the Proprietary lubricants.

Recent research on High Performance Premixes

Engineers at Rio Tinto Metal Powders, Canada, and Metalsinter S.r.l have been working closely to optimize the compaction stage of Powder Metallurgy process. A high performance premix has been reported as a method to increase compaction speed while maintain excellent surface finish. [7]

In order to optimize, accelerate, compaction process the powder mix should have the right flow properties to adequately fill the die, avoid entrapped air, cause green cracks and improve part weight stability.

In this study, the compaction of a water pump pulley manufactured by Metalsinter S.r.l, Italy was performed using three powder mixes containing high performance lubricants. The compaction was compared to the regular production premix used at Metalsinter for the same part. The objective was to demonstrate how a high performance premix can lead to increased production rates while maintain quality output from the process as shown in Table 5.

Table 5. Composition of powder mixes tested under industrial conditions.[7]

Powder sample	Base	Cu (w/w%)	C (w/w%)	Lubricant (w/w%)	Apparent density (g/cm ³)	Flow Rate (s/50g) (Hall/Gustavsson)
A	AT-1001	1.0% AcuPowder 165G	0.5% Timal PG-25	0.8% Caplube L	3.11	27 / 33
B				0.8% Apex Mid-Dens	2.76	31 / 35
C				0.8% PR-2B	2.92	33 / 39

Caplube-L: Manufactured by Blachford, Canada; Apex Mid-Dens: Apex Advanced Technologies, USA; PR2B: proprietary lubricant developed by Rio Tinto Metal Powders.

It can be seen that Apparent Densities vary significantly. A lower AD gives a higher die fill, this in turn makes the compaction cycle longer. A higher Apparent density is therefore a desirable feature of a high performance mix. In the green state the main feature driving quality of the surface finish is lubrication performance as shown in Fig 4.

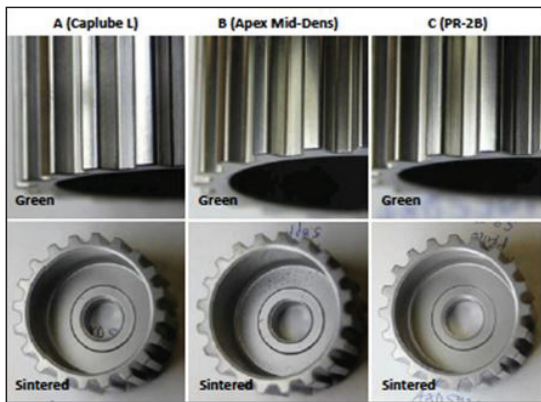


Fig. 4 Evaluation of green and Sintered aspect in normal production conditions and Regular sintering[7]

The study demonstrated each lubricant offered advantages in some key aspects, e.g. part cleanliness, maximized stroke rate, increased compressibility or more stable part weights. The lab measurement of flow rate did not correlate with part weight stability. Selection of lubricant has to be made keeping in mind each part production process as shown in Table 6.

Table 6. Summary of trials showing benefit of using High Performance Lubricants to optimize compaction of PM parts [7]. DFS-Die fill Sequence.

	Reference	Powder mixes				
		Mix A (Caplube L)	Mix B (Apex Mid-Dens)	Mix C (PR-2B)		
Compaction optimisation	Optimal DFS	DFS-STD	DFS-3	DFS-1	DFS-2	
	Speed	S	5S	5S	5S	
	Shakes	N	N	0.5N	N	
	Dwell time	DT	0.38DT	0.75DT	0.75DT	
	Shake duration	T	0.6T	0.6T	0.6T	
	Stroke rate [ppm]	5.9	7.5	7.3	7.2	
	Compaction speed improvement vs reference [%]	N/A	+27%	+24%	+22%	
	Stability results	Hall flow rate [s/50g]	N/A	27	31	33
		σ (g)	0.31	0.87	0.58	0.67
		σ_c (%)	0.69	1.94	1.28	1.49
σ_c (%) [constant filling height]		0.63	1.66	0.98	1.43	
Die-fill adjustments [number per 1,000 parts]		35	85	90	57	
Surface finish	Qualitative observation Green state [ranking]	N/A	Comparable			
	Qualitative observation Sintered state [ranking]	N/A	Second	Last	Best	

Conclusion

As the parts become more complicated, the Raw Material becomes application specific, to meet the needs of makers of Powder Metal parts. There are a wide variety of choices in terms of Premixes, Dust free mixes, mixes for Warm Die compaction and cost effective “Organic bonded mixes”.

One only needs to state what he wants and the Powder Metal Material Technologists can readily suggest what he needs.

References:

1. Research and Markets- Global overview Report 2018.
2. JFE Metal powders- Brochure ; Page 2 and Page 3.
3. Distaloy AQ- September, 2016, Hoganas publication 1587.

4. *Sylvain St-Laurent and Julie Campbell , Rio Tinto Metal powders. Powder Metallurgy Review Winter 2014 Page 68-70.*
5. *“Lubricants for compaction of a PM part”; Matts Larsson , and Maria Ramstedt, Hoganas AB, Sweden.*
6. *“Double Press Double Sinter Alternatives for High Density Applications” Alex Wartenberg and Chris Schade, Hoeganaes Corporation, Cinnaminson, NJ 08077.*
7. *“High-performance premixes for increased production rates and optimum surface finish” Paris, Research Engineer-Product development, Rio Tinto Metal Powders, Canada, Powder Metallurgy Review, Spring 2018, Pages 61-70*

MATERIAL OPTIONS FOR HIGH TEMPERATURE SINTERING

Kylan McQuaig, Neal Kraus, Bruce Lindsley

Hoeganaes Corporation, Cinnaminson, NJ, USA.

Abstract: Materials such as Fe-Cu-C steels are commonly used in the PM industry and offer a good combination of cost and mechanical properties. For elevated strength and ductility applications, however, higher alloy steels are required. Traditionally, this has meant adding Mo and Ni as alloying elements. Alternative alloying systems incorporating Cr, Si and V for ferrous PM are being developed to address price, environmental and recyclability concerns. Several material options are explored and the potential increase in mechanical properties via high temperature sintering is outlined.

Introduction

The powder metallurgy (PM) industry is constantly evolving and adapting to changing market trends. As vehicle light weighting becomes more prevalent in the automotive industry and material property demands become more extreme, advanced material options and processing techniques must be developed to meet these needs.

Mechanical properties in PM materials can be increased in several ways, including increasing overall alloy content, raising part density, and/or improving degree of sinter. Increasing alloy content is an attractive option to improve part performance, as it requires little or no change in the subsequent processing operations. But raw material price fluctuation makes this approach riskier than the alternative options. Common PM alloying elements such as molybdenum and nickel have seen substantial price volatility over the past decade [1-3]. Material pricing from the LME Index is shown in Fig. 1.

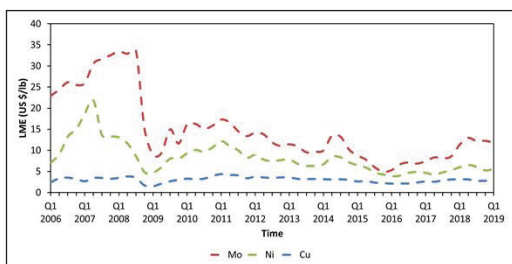


Fig. 1: LME Index material costs from 2006-2019^[4].

Compacting parts to higher green density is another viable approach, as this results in comparably processed parts with both higher strength and ductility. Double press double sinter (DPDS) processing has been utilized for many years but necessitates the need for a substantial amount of additional processing. Advanced lubricant options make high density compaction possible in a single step but may require specialized press capabilities as well as potentially higher material cost [5-7].

The use of high temperature sintering is another alternative, allowing for the use of unique alloying elements to achieve similar mechanical properties. With the introduction of improved sintering techniques and through use of high temperature sintering, elements such as manganese, silicon, vanadium, and chromium can be used to replace significantly higher amounts of “standard” PM elements such as nickel and molybdenum [2,3,8-13]. Fig. 2 below shows the relationship between oxygen partial pressure and temperature on the stability of some common metal oxides [14]. These alternative alloying elements, which have not been used historically in the PM industry due to their stable oxide formation, become extremely attractive when used in conjunction with high temperature sintering thanks to their effectiveness at relatively low alloy additions.

MATERIAL OPTIONS FOR HIGH TEMPERATURE SINTERING

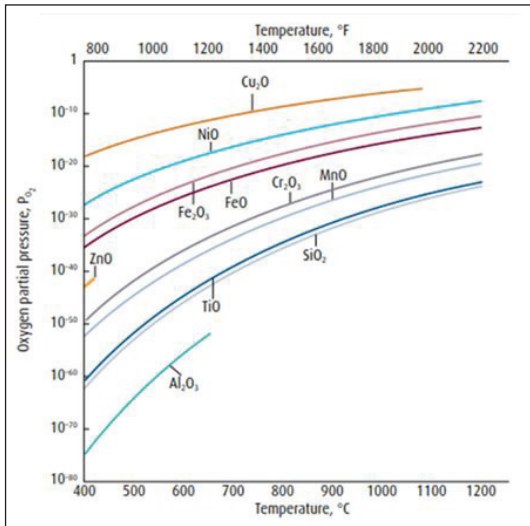


Fig. 2: Relationship between oxygen partial pressure and temperature for metal/metal oxide equilibrium [14]

The high temperature sintering approach can be utilized in several different ways, as will be explored in this study. The use of alternative alloying elements presents an opportunity to remove more expensive and highly-regulated alloying elements, such as nickel, from PM alloys [15-16]. Alternatively, mechanical properties can be achieved that are superior to those typically observed in standard PM materials, or leaner alloys can be utilized to drive down material cost while maintaining necessary part performance.

Experimental Procedure

For this study, powder premixes were made using the nominal compositions as shown in Table I. Five “standard” PM compositions were used to determine the benefit of high temperature sintering on common alloys. These compositions are listed by their MPIF standard designation, except for the Ancorsteel™ 4300 material, which does not have a designation and will be referred to by its trade name [17]. Two specially designed high temperature sintering (HTS) alloys utilizing alternative alloying

elements of silicon and vanadium were also studied. All premixes in this study were made using commercially-available water atomized base iron from Hoeganaes Corporation and standard PM alloying additives. All mixes contained 0.75% EBS wax as the lubricant.

Table I: Nominal compositions of premixes explored in this study

MPIF Designation (if applicable)	Fe (%)	Mo (%)	Ni (%)	Cu (%)	Mn (%)	P (%)	Cr (%)	Si (%)	V (%)	C (%)
FY-4500	Bal.	—	—	—	—	0.45	—	—	—	—
FC-0205	Bal.	—	—	2.00	—	—	—	—	—	0.60
FLN2C-4005	Bal.	0.50	1.75	1.50	—	—	—	—	—	0.60
Ancorsteel 4300	Bal.	0.85	1.00	—	—	—	1.00	0.60	—	0.60
FLC2-4808	Bal.	1.25	1.40	2.00	0.40	—	—	—	—	0.60
HTS #1	Bal.	—	—	—	—	—	—	0.75	—	0.90
HTS #2	Bal.	—	—	—	—	—	—	0.60	0.16	1.10

All laboratory testing was carried out in accordance with the appropriate MPIF standards [17]. Mechanical properties were measured using transverse rupture (TR), dogbone tensile, and Charpy impact samples compacted to green density of 7.0 g/cm³ at room temperature. These samples were sintered for approximately 20 minutes at temperature in a mixed atmosphere of nitrogen and hydrogen (FY-4500 sintered in 100% hydrogen). The mechanical properties of each premix were evaluated on sets of five bars for each test performed.

Results

All measured mechanical properties in this study are summarized in Table II. All five standard PM material grades were tested both in a “standard” sintering condition (1120 °C except for the Ancorsteel 4300 material) as well as a high temperature condition of 1260 °C. The HTS alloys are expected to be most effective at high temperature and were, therefore, only sintered at 1260 °C due to the unique alloying elements utilized. As expected, all materials in this study saw increases (to varying degrees) in strength, hardness, elongation, and impact energy following high temperature sintering.

MATERIAL OPTIONS FOR HIGH TEMPERATURE SINTERING

Table II: Summary of mechanical properties of all 7 mixes studied

Mix Type	Sintering Temperature	Apparent Hardness (HRA)	UTS (MPa)	Elongation (%)	Impact Energy (J)
FY-4500	1120	35	353	12.7	45
	1260	37	373	16.7	81
FC-0205	1120	48	503	2.7	15
	1260	49	520	2.8	16
FLN2C-4005	1120	57	667	2.0	18
	1260	57	715	2.3	19
Ancorsteel 4300	1180	69	1009	1.1	16
	1260	70	1278	1.8	23
FLC2-4808	1120	67	946	1.1	14
	1260	67	1063	1.5	18
HTS#1	1260	52	652	3.8	23
HTS#2	1260	60	738	1.8	18

Focusing on the FY-4500 material, sintered in 100% hydrogen, a substantial increase in mechanical properties is observed. Ductility (31%) and impact energy (76%) dramatically increase following high temperature sintering. The accompanying etched microstructures for this alloy can be seen in Figures 3A and 3B. High temperature sintering this material results in a significant amount of pore-rounding and a much larger ferrite grain size. For phosphorus-containing materials such as FY-4500, contamination prevention and sintering with a higher hydrogen content are vital, as carbon, oxygen, and nitrogen are all known to be detrimental to both mechanical and soft magnetic properties of the sintered components^[18].

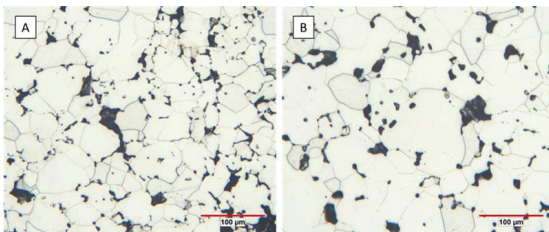


Fig. 3: Etched microstructures for FY-4500 sintered at 1120 °C (A) and 1260 °C (B)

For other common PM materials, the increase in mechanical properties with high temperature sintering is not nearly as pronounced. An increase in ultimate tensile strength was observed in each material, but none of the five “standard” materials outside of FY-4500 and Ancorsteel 4300 experienced a strength increase

greater than 15%. The two premixes containing admixed copper, FC-0205 and FLN2C-4005, saw only minor improvements in properties across the entire temperature range. The etched microstructures of FC-0205 can be seen in Figures 4. While the pore rounding is present in all high temperature sintered materials, the microstructural constituents are similar when looking at these two materials, with little difference observed when comparing the two sintering temperatures. However, higher Ni versions of FLNC type alloys are available and it is known that admixed Ni diffuses better at higher temperatures. Therefore a study on the effect of sintering temperature over a range of Ni contents for these Mo-Ni-Cu alloys was undertaken. Figure 5 shows the increase in UTS with increasing Ni content. Again, at low Ni content, little benefit is found with higher sintering temperatures. With Ni contents of 2% and greater, a significant increase in strength is observed. For alloy FLN4C-4005, a 29% increase in UTS is observed with high temperature sintering. More benefit from higher Ni contents is realized with high temperature sintering.

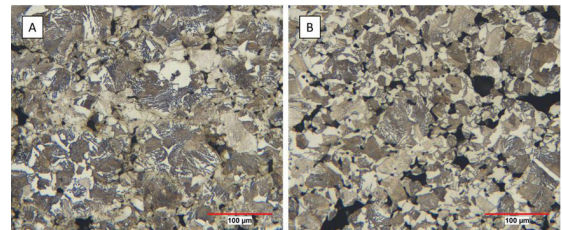


Fig. 4: Etched microstructures for FC-0205 sintered at 1120 °C (A) and 1260 °C (B)

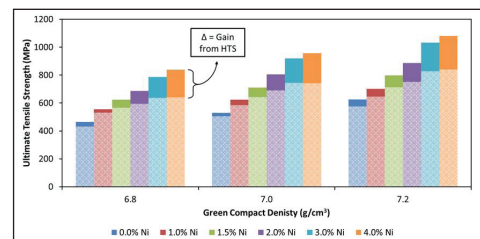


Fig. 5: Effect of Ni content and sintering temperature on UTS strength of FLNXC-4005 type alloys. Hashed bars are 1120 °C sintering, dark bars are 1260 °C sintering.

MATERIAL OPTIONS FOR HIGH TEMPERATURE SINTERING

The next of the “standard” alloys tested was the first sinter-hardening alloy used in this study, Ancorsteel 4300, which contains nickel, chromium, and silicon in addition to the prealloyed molybdenum base iron. This material utilizes some of the same elements as the HTS alloys and, with these alloying elements present, it would be expected to perform very well with high temperature sintering. A more uniform microstructure can be observed (Figures 6A and 6B), which accompanies a dramatic improvement in strength, elongation, and impact due to a more uniform diffusion of the alloying elements. Figure 6A shows the etched microstructure of the sinter-hardened material sintered at 1180 °C, with martensite, large islands of bainite, and a number of nickel-rich areas where the Ni is more highly concentrated. In contrast, Figure 6B has a much higher percentage of martensite and more thorough diffusion of the nickel has taken place.

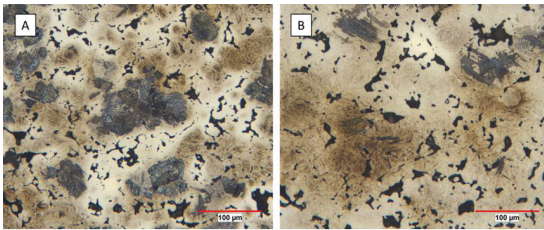


Fig. 6: Etched microstructures for Ancorsteel 4300 sintered at 1180 °C (A) and 1260 °C (B)

The same trends did not hold true when high temperature sintering the other sinter-hardening material, FLC2-4808. While the elongation and impact do increase somewhat, there is almost no increase in strength and both sets of samples were found to have a fully martensitic microstructure as shown in Figures 7A and 7B.

Similar to the Ancorsteel 4300 material, the HTS alloys reach optimal properties through high temperature sintering. Each material showed a good combination of strength and ductility in the final properties. Figure 8 shows the typical pearlitic microstructure that was observed for each of the HTS alloys. As shown in the figure, the lamellar spacing of the pearlite is extremely

fine. The presence of silicon and vanadium in these alloys strengthens and refines the microstructure, while also preventing the formation of grain-boundary carbides, even with the 1.1% graphite addition in HTS #2.

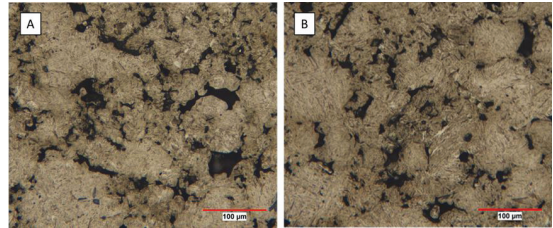


Fig. 7: Etched microstructures for FLC2-4808 sintered at 1120 °C (A) and 1260 °C (B)

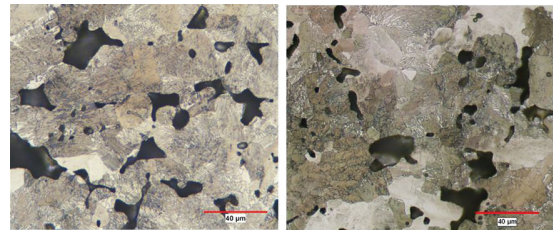


Fig. 8: Etched microstructure of HTS #1 (A) and HTS #2 (B) sintered at 1260 °C

Discussion:

Regarding the standard PM alloys, the largest improvements were in elongation and impact energy following high temperature sintering. Table III shows the percent increase in each property for a given material type when increasing sintering temperature from the “standard” to 1260 °C. Two of the copper-containing steels, FC-0205 and FLN2C-4005 exhibited little benefit with high temperature sintering. Copper is utilized in powder metallurgy because it melts at standard sintering temperatures, allowing for more rapid liquid-phase sintering and strengthening of the particle necks. For this type of material, clearly high temperature sintering does not provide as great a benefit compared to other common PM alloys. Interestingly, the copper-containing sinter-hardening grade FLC2-4808, did show a larger benefit, and it is thought

MATERIAL OPTIONS FOR HIGH TEMPERATURE SINTERING

the martensitic microstructure is more sensitive to the sinter quality. The largest improvement in properties was found with the Ancorsteel 4300. This martensitic material benefits in a similar way to the FLC2-4808, and additionally, the microstructure becomes more uniform with more homogenous alloy distribution.

Table III: Percentage improvement in property following high temperature sintering

Mix Type	UTS (%)	Elongation (%)	Impact Energy (%)
FY-4500	6	31	82
FC-0205	3	4	9
FLNC-4005	7	15	8
Ancorsteel 4300	27	64	42
FLC2-4808	12	36	30

To highlight the mechanical properties achievable with the HTS alloys, Table IV shows UTS and impact energy as well as total alloy content, compared with a standard alloy system. The standard alloy chosen, FLN2C-4005, would be considered a “high-end” material in the PM industry in terms of alloy content, material properties, and cost. The HTS alloys, each utilizing an unalloyed iron base and less than 2% total alloy content, can essentially match both strength and ductility of these alloys when used in conjunction with high temperature sintering. The investment in high temperature sintering in combination with these low alloy materials can therefore insulate component makers from potential alloying element price spikes in the future.

Table IV: Properties achieved at 1260 °C for select mixes compared to total alloy content

Mix Type	UTS (MPa)	Impact Energy (J)	Total Alloy (%)
FLN2C-4005	715	19	4.35
HTS#1	652	23	1.65
HTS#2	738	18	1.86

Conclusions

As a result of the experimental work performed during this study, the following observations were made:

- High temperature sintering increases the strength, elongation, and impact energy of all

alloys tested in this study as a result of pore round and improved degree of sinter.

- Certain properties, such as elongation and impact energy, improved dramatically in most materials, while strength was more material-dependent. In applications where maximizing material ductility and toughness are desired, high temperature sintering is most beneficial.
- Materials containing admixed copper saw only a marginal improvement as a result of high temperature sintering. Sinter-hardening grades appear to be an exception to this observation.
- Silicon and vanadium were effective at refining material microstructure and preventing carbide formation, even at high graphite additions.
- Alloying elements such as Si and V can be utilized to achieve properties equivalent to more highly alloyed PM materials, providing a route for leaner materials and cost savings through improved processing. The elements also provide a route to nickel-free alloys if desired. The combination of silicon with additional alloying elements yields an excellent combination of strength and ductility in Ancorsteel 4300.

Acknowledgements

The authors want to thank Meghan Fields, Jeanne Falzone, Eric Alesczyk, and Barry Diamond for all their contributions to this manuscript.

References

1. *Nickel price soars amid export ban and sanction fear*, Powder Metallurgy Review, (2014), Vol. 3, No. 2, p. 10.
2. *B. Lindsley, High performance manganese containing PM steels*, Advances in Powder Metallurgy & Particulate Materials, compiled by R. Lawcock, A. Lawley and P. J. McGeehan, MPIF, Princeton, NJ, (2008), part 7, p. 17-25.

MATERIAL OPTIONS FOR HIGH TEMPERATURE SINTERING

3. B. Lindsley, W.B. James, *PM steels that contain Mn, Advances in Powder Metallurgy & Particulate Materials*, compiled M. Bulger and B. Stebick, Metal Powder Industries Federation, Princeton, NJ, (2010), part 10, p. 36-49.
4. London Metal Exchange, (2019), Online, Available: <https://www.lme.com/Metals>.
5. H. Rutz, F. Hanejko, *High Density Processing of High Performance Ferrous Materials, Advances in Powder Metallurgy & Particulate Materials – 1994*, compiled by C. Lall and A. Neupaver, Metal Powder Industries Federation, Princeton, NJ, 1994, Vol. 5, pp. 117-133.
6. F. Hanejko, *Warm Die Compaction with Reduced Lubricant Levels Promoting Higher Green and Sintered Densities*, APMA 3rd International Conference on Powder Metallurgy, Kyoto, Japan, (2015).
7. A. Wartenberg, C. Schade, *Double Press Double Sinter Alternatives for High Density Applications, Advances in Powder Metallurgy & Particulate Materials*, Vol. 1, p. 266-275, (2017).
8. P. King, *Chromium Containing Materials for High Strength – High Fatigue Applications*, PM World Congress Proceedings (2004).
9. C. Schade, T. Murphy, A. Lawley, R. Doherty, *Microstructure and Mechanical Properties of PM Steels Alloyed with Silicon and Vanadium*, *International Journal of Powder Metallurgy*, (2012), 48/6, p. 41-48.
10. B. Lindsley, C. Schade, T. Murphy, *Vanadium and Silicon Alloyed PM Steels*, Euro PM Congress Proceedings (2013).
11. C. Schade, T. Murphy, A. Lawley, and R. Doherty, *The Influence of Silicon on the Mechanical Properties and Hardenability of PM Steels*, *Advances in Powder Metallurgy and Particulate Materials*, (2013), compiled by D. Christopherson and R.M. Gasior, MPIF, NJ, vol. 7, pp. 54-72.
12. C. Schade, T. Murphy, , A. Lawley, R. Doherty, *Microstructure and Mechanical Properties of a Bainitic Powder Metallurgy Steel*, *International Journal of Powder Metallurgy*, (2016), Vol. 52, No. 2, p37-46.
13. D. Milligan, U. Engstrom, S. Smith, *High Temperature Sintering – a Cost Effective Way to Future High Performance Materials*, PM2TEC2005 Proceedings, Montreal, Canada, (2005).
14. *Furnace atmospheres no. 6: Sintering of steels*, The Linde Group.
15. B. Neumann, G. Kotthoff, V. Arnhold, *REACH: Risks, challenges and opportunities for sintered parts manufacturers*, published in *Pulvermetallurgie in Wissenschaft und Praxis*, Vol. 28, (2012).
16. J. Khambekar, B. Pittenger, *Understanding and Preventing Metal-Dust Hazards*, *International Journal of Powder Metallurgy*, Vol. 49, Issue 4, (2013).
17. *Standard Test Methods for Metal Powders and Powder Metallurgy*, Metal Powder Industries Federation, Princeton, NJ, 2016 Edition.
18. K. Sunday, K. McQuaig, *Effect of Impurities on Aging of Sintered Soft Magnetic Materials*, Presented at: PowderMet 2018, San Antonio Texas, (2018).

IMPROVEMENT OF MECHANICAL PROPERTIES OF AlCoCrFeNiSi HIGH ENTROPY ALLOY BY Ni ADDITIVE SINTERING

Sahil Rohila, Subhendu Naskar, Bharat B. Panigrahi*

Department of Materials Science and Metallurgical Engineering,
Indian Institute of Technology Hyderabad, India.

Abstract: HEAs have higher strength, stability and inertness toward the active corrosion environment over a wide range of temperatures as compared to the other conventional alloys. Among HEAs, Al-based HEAs show good combination of strength with lighter weight, such as AlCoCrFeNi, AlCoCrFeNiSi, AlCoCrFeNiTi_{0.5}, and AlCoCrFeNi_{2.1}. Among them, AlCoCrFeNiSi shows very high hardness and superior specific strength, however it lacks required ductility. The focus of present work is to achieve higher strength and to improve its plastic strain. Ni has been used as a sintering aid as well as binding phase. Elemental Ni powder was mixed with the mechanically pre-alloyed AlCoCrFeNiSi HEA powder and hot-pressed at 1200°C. Compression test reveals, about 10 wt.% Ni addition lifts the strength to about 3.04 GPa, which was about 72% jump from the base alloy. This ultra-high strength value was accompanied with a reasonable plastic strain.

1. Introduction

Entropy is one of the significant factors which defines the stability of the system. Higher entropy yields the system toward stability, i.e., minimum Gibbs free energy. Alloys with configurational entropy higher than $1.5R$ (R = Gas Constant) are considered stable and are called High Entropy Alloys (HEAs). HEAs are the simple solid solution of 5 or more elements in an equiatomic or nearly equiatomic proportion [1], [2]. HEAs remain stable over a wide range of temperatures and corrosive environments. HEAs possess high hardness, high strength, better wear, and creep resistance, with superior thermal and chemical stability [2]-[4]. Such properties of HEAs have attracted many scholars for the past two decades. HEAs could be the potential futuristic materials that may substitute many of the present super-alloys. HEAs have the distorted lattice, which hinders the movement of atoms or vacancy, and hence leads to sluggish diffusion. A large amount of energy is required to displace an atom or vacancy; hence it shows high strength [2], [3], [5], [6]. Each lattice acts as a multi-elemental nano-

scale composite, which provides the combined effect of properties from all elements: primarily known as cocktail effect [1]-[3], [7]. HEAs appeared to be suitable for tools, transportation, aerospace, energy sector, and applications with extreme working conditions.

HEAs can be fabricated through melting-casting, powder metallurgy, additive manufacturing, and other conventional techniques. Irrespective of the processing techniques, HEAs majorly condense as BCC, FCC, or a combination of both the phases [1], [8]. Few HEAs also show the presence of additional sigma or laves phase in the matrix [9]-[12]. Early reports emphasized the single-phase HEAs, but later developments in the field, also include mixed-phase HEAs [13]. Melting-casting and mechanical alloying are the two primary methods to produce HEAs. In melting-casting, elements need to be re-melted several times to achieve homogeneity in composition. Elements having a large difference in melting points and high mixing enthalpy tends to segregate and form additional compounds or phases [14]. Whereas in mechanical alloying, elemental

IMPROVEMENT OF MECHANICAL PROPERTIES OF AlCoCrFeNiSi HIGH ENTROPY ALLOY BY Ni ADDITIVE SINTERING

powders are ball-milled in the presence of milling media. Powder undergoes multiple fractures and cold-welding continuously for long hours. Mechanical alloying generally takes long processing time to produce an alloy, but it provides extended solubility at lower temperatures^{[15],[16]}. So, alloys which are difficult to produce through melting casting or any other technique, can be easily produced through mechanical alloying. Spark Plasma Sintering (SPS), hot isostatic pressing (HIP), and hot press are the standard techniques to obtain high-density alloys. In all these processes, external pressure is applied at elevated temperatures to combine plastic deformation and diffusion, to enhance densification.

Ni, Co, and W based super-alloys are common materials for high-temperature applications due to their high creep performance, phase stability, and high strength. Al-based high entropy alloys show much higher specific strength. HEAs can reduce the overall weight of the machine's component and can improve efficiency effectively. Effect of Si has been studied over the past many years in conventional alloys (Al and Fe based alloys) due to its specific alloying behavior. A small addition of Si can improve the strength and corrosion resistance of the system effectively^{[17]-[19]}. Similar effects have been observed in the HEA as well. AlCoCrFeNi is one of the most studied HEA, crystallizes with FCC and BCC phases^{[16],[20]}. It shows a good combination of strength and ductility amongst HEAs. Addition of Si stabilizes the BCC phase and increases compressive strength up to 2.9GPa from 2.4GPa^{[21],[22]}. AlCoCrFeNiSi is one of the least studied HEA due to its tendency to form oxides and metallic glass.

In comparison to superalloys, AlCoCrFeNiSi shows higher specific strength, higher hardness, and better corrosion behavior^{[21],[23],[24]}. AlCoCrFeNiSi shows brittle fracture and does not show prior indication to failure, which

makes the alloy difficult to use in industries or to commercialize. Materials with high hardness and strength have high potential in the tool cutting and machining industries, but lack of toughness limits its application. The present study focuses on improving the strength and plastic strain of AlCoCrFeNiSi by reinforcing soft Ni phase into the matrix. The present investigation aims to study the effect of nickel addition on AlCoCrFeNiSi HEA powder on the densification behavior and mechanical properties. It is expected that nickel being a softer phase, may impart ductility and toughness in the alloy.

2. Experimental

High purity elemental powders of Al, Co, Cr, Fe, Ni, and Si were taken in an equiatomic proportion on a planetary ball mill (Pulverisette-5, Fritsch, Idar-Oberstein, Germany). Vials and balls of tungsten carbide were used to mill the powder, with the ball to powder weight ratio of 15:1. Toluene was used as a process agent to avoid heat and oxidation during the process. Milling was performed at 300 rpm for 20h with an intermittent pause to prevent excessive heating. Milling for 20h was done in 40 cycles, and each cycle has 30 minutes of milling and 60 minutes of pause time to cool down. Alloyed powder with toluene was dried through natural evaporation in a closed fume hood. Further, three different sets of powders were prepared by adding 0% (without Ni), 5%, and 10% by weight, high purity Ni powder to the pre-mechanically alloyed AlCoCrFeNiSi (HEA) powder, and designated as 0Ni, 5Ni and 10Ni samples. Mixing was done at a speed of 70 rpm for 1 hour with the ball to powder weight ratio of 5:1 in toluene. Mixed powders were kept in an inert atmosphere to avoid oxidation.

Graphite die of about 20 mm diameter was used to sinter the samples. Hot press (VB Ceramics) was done at 1200°C with a heating rate of 10 °C per minute. About 52 MPa of uniaxial pressure was applied at 1200°C and held isothermally

IMPROVEMENT OF MECHANICAL PROPERTIES OF AlCoCrFeNiSi HIGH ENTROPY ALLOY BY Ni ADDITIVE SINTERING

for 60 minutes. The density of all the sintered samples was measured by Archimedes setup and compared to the theoretical density. Sintered samples were polished using various grids of SiC paper gradually from 180 to 2000 and then followed by fine alumina and diamond polishing. Polished samples were etched using 40% aqua regia in methanol to obtain the microstructure. To understand the phase formation, X-ray diffraction (XRD Rigaku Ultima IV) of the milled powder and sintered samples were done using Cu $\kappa\alpha$ radiation with a step size of 0.7° per minute. Microstructures were characterized using the Field emission scanning electron microscope (FESEM, JSM-7800F, JEOL) equipped with EDS (EDAX- Octane Elite) at 20kV. Micro-hardness (EMCO Test DuraScan G5, Kuchl, Austria) of the samples was performed at 20 N with the dwell period of 10 sec; and at least 20 readings were taken for each sample at each load to verify the micro-hardness. Samples for compressive testing were cut through the wire EDM with an aspect ratio of 1.5-1.6 (l/D ratio). The compressive strength was tested at a strain rate of 10-3 sec⁻¹ using Instron testing machine.

3. Results and discussion

3.1 Phases and microstructures

Figure 1 shows the XRD patterns of the as-milled powder and sintered samples. After milling, AlCoCrFeNiSi crystallizes with the combination of BCC and FCC phases. Additional alpha (α) and B2 phases are observed as smaller peaks, along with the major phases. High lattice strain is accumulated during milling; hence peaks of as-milled powder are broader and shorter. High energy ball milling also yields to the formation of metastable phases, which tend to stabilize during sintering. The primary BCC phase was reported to be retained after the sintering of samples [24]-[26]. Sintered AlCoCrFeNiSi shows a primary BCC phase with minor peaks of FCC, alpha (α), and B2 phases. Peaks become more refined and sharper, exhibiting complete crystallization

of HEA. The additions of 5% and 10% Ni have an inconsequential effect on the base phase. Ni added samples (5Ni and 10Ni) show BCC as a major phase; along with small peaks of FCC, α , and sigma (σ) phases. The addition of Ni favors the formation of Fe-Cr rich σ phase [27].

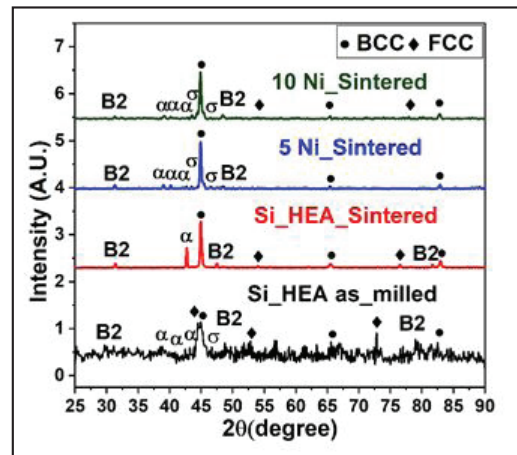


Fig. 1. XRD patterns of AlCoCrFeNiSi as-milled powder and all sintered samples.

Figure 2 represents the SEM micrographs and EDS patterns of all the three sintered samples. Alloys are observed to have a combination of multiple phases, as visible from the variable contrast of the SEM microstructures. In the microstructure matrix region is represented by (1), precipitates are represented by (2), bright lamellas are represented by (3) and black lamellas represented by (4). Figures 2a and 2 \bar{a} show the SEM and EDS of 0Ni sample, which shows two different regions in the microstructure. Light grey (Cr rich) precipitates (region 2) are observed on the continuous dark grey (Co-Ni rich) matrix (region1). Few researchers have also obtained similar morphologies in as-cast and sintered AlCoCrFeNi microstructure [28]. Figure 2 \bar{a} shows the higher resolution image, which also shows similar microstructure. The size of the Cr rich precipitates (region 2) varies between 1-10 μ m. Small-sized precipitates are irregular in

IMPROVEMENT OF MECHANICAL PROPERTIES OF AlCoCrFeNiSi HIGH ENTROPY ALLOY BY Ni ADDITIVE SINTERING

shape, whereas large-sized precipitates are of globular shape. All precipitates (2) are found to have round edges; no sharp-edged precipitates are observed in the matrix (1). Few black colored carbon-rich regions (4) are also observed in the microstructure as Si has a high affinity towards carbon and oxygen to form carbides and oxides. All other elements are found to be distributed nearly equally.

Figures 2b and 2̄ show the SEM micrographs and EDS analysis of 5Ni sample. Figure 2b shows the microstructure contains precipitates of variable size, fiber shaped rod like lamella structure (3), higher magnification also reveals the presence of black lamellas structure (4) over the precipitates (2). The basic morphology of Cr-rich precipitates (2) in Co-Ni rich matrix (1) remains the same. But precipitates transform from globular to lamellar structure, and a higher proportion of sharp-edged fine precipitates are observed. Few new attributes are also observed along with the basic morphology, rod lamella structure (3) and black lamella (4). EDS pattern shows that the rod lamella (4) is a Cr-rich phase, same as the bright precipitates (2) in 0Ni sample and the black lamellas (4) are Ni-rich. The fraction of small-sized precipitates and large-sized precipitates (2) decreases in comparison to the 0Ni sample.

Figure 2c and 2̄ shows SEM and EDS composition of 10Ni sample, which has almost similar microstructure to that of 5Ni sample, with some minor modification. Figure 2c shows the two different types of regions; first, a uniform and homogenous phase, combination of precipitates and matrix (A), and the second region with segregation of precipitates (B). Precipitate density (precipitates per unit area) decreases, and grains of the matrix appear to be more organized and interconnected. Few fine-sized precipitates are observed in the grain boundaries of the matrix (C). The presence of segregation and precipitation regions are found periodically. The amount of fine precipitates (2) decreases compared to 5Ni sample, and the edges of the precipitates become globular. Higher resolution image, figure 2̄ shows the higher amount of black lamellas over the precipitate surface and an interconnectivity of large-sized precipitates has been noticed, which shows the overall morphology of the system to be lamella. The shape of the precipitates changes back to globular (2) from sharp lamella (3).

3.2 Densification

Figure 3 shows the dilatometer curves of 0Ni and 10Ni samples. 0Ni sample shows the shrinkage of about 7.3% at 1300°C, whereas addition of Ni (10Ni) has increased marginally the linear shrinkage to about 8.3% under pressureless sintering condition. Figure 4 shows the absolute and relative densities of the sintered samples, sintered (hot pressed) at 1200°C, which are nearly same for all samples. All samples show higher relative density (greater than 96%) through hot press sintering.

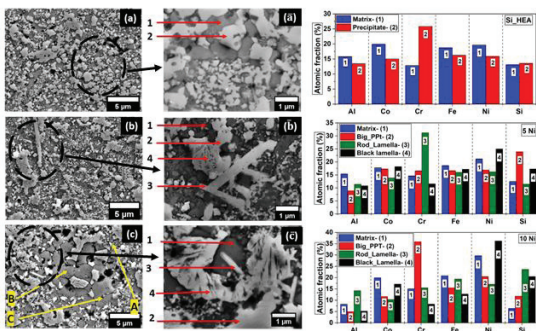


Fig. 2 SEM micrographs and respective EDS analysis of various sintered samples: a) 0Ni, b) 5Ni and c) 10Ni.

IMPROVEMENT OF MECHANICAL PROPERTIES OF AlCoCrFeNiSi HIGH ENTROPY ALLOY BY Ni ADDITIVE SINTERING

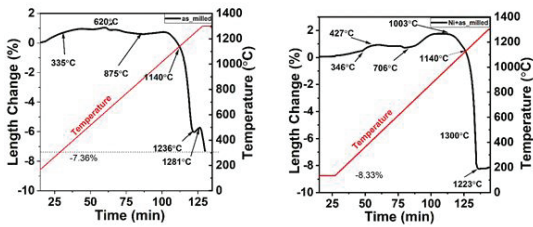


Fig. 3. Dilatometer curves of: (a) as-milled AlCoCrFeNiSi and (b) AlCoCrFeNiSi+10%Ni.

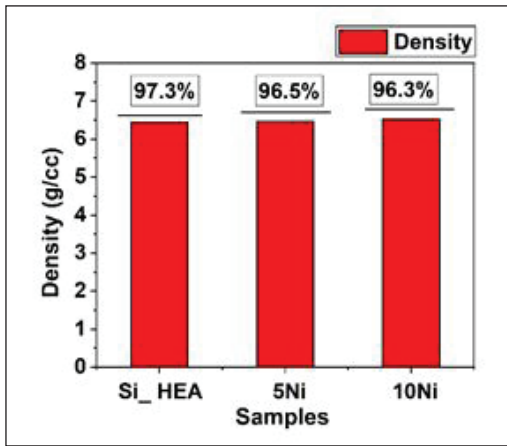


Fig. 4 Sintered densities (with relative densities in %) of 0Ni, 5Ni and 10Ni samples.

3.3 Mechanical properties

The hardness of the samples has been shown in Figure 5, where hardness seems to be slightly increased by Ni addition. Hot pressed 0Ni shows 1092 ± 58 HV and 5Ni sample shows 1133 ± 39 HV, which are higher than the reported 1009HV, 908HV through as-cast and SPS samples [26], [29].

Stress-strain profile of the samples tested under compressive loading have been shown in Figure 6. The compressive test shows an improvement in the strength from 1.77GPa (for 0Ni) to 3.047GPa (for 10Ni). 0Ni sample exhibits a plastic strain of about 1.5%, which increased to 2.35% and 3.1%

with 5 and 10% Ni additions respectively. On the whole, addition of Ni improves the strength by 72% (with 10% Ni) and plastic strain by 106%.

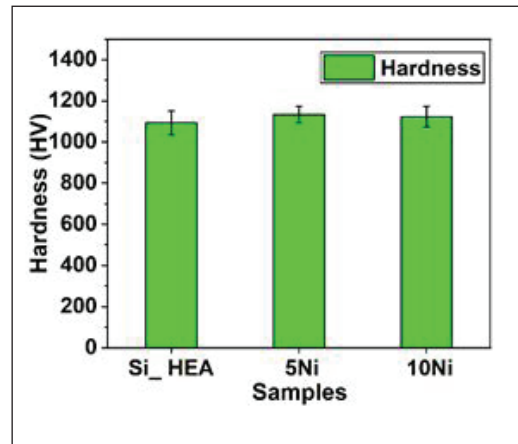


Fig. 5 Hardness of 0Ni, 5Ni and 10Ni samples

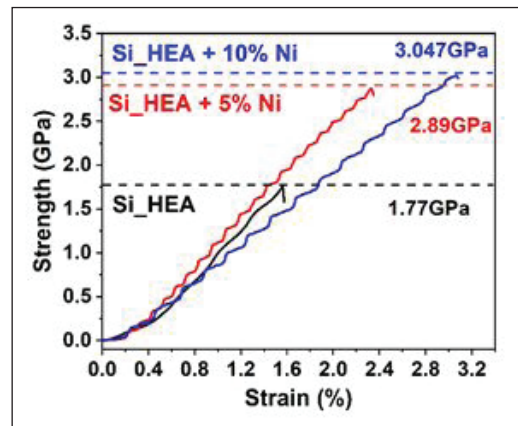


Fig. 6 Stress strain data obtained for compressive strength testing

4. Discussion:

After milling, AlCoCrFeNiSi HEA crystallizes with majorly BCC phase. Broader peaks are observed due to the accumulation of strain during milling. The presence of Si and Fe-Cr in an alloy tends to form α and σ based intermetallic compounds. Metastable phases are also observed during milling. Upon sintering, AlCoCrFeNiSi

IMPROVEMENT OF MECHANICAL PROPERTIES OF AlCoCrFeNiSi HIGH ENTROPY ALLOY BY Ni ADDITIVE SINTERING

crystallizes with major BCC phase and some minor FCC and α phases. Verification of the α phase has been done by calculating the negative enthalpy and Gibbs free energy of formation of possible binary and ternary compounds using Thermo-Calc software. JCPDF data of such potential compounds matched with the current XRD and further, the EDS compositional analysis and confirmation of the phases.

Table 1 shows the negative enthalpy of all elements with respect to each other. Si is more likely to form phase with Ni, Co, and Cr. Total Gibbs free energy of the formation of AlCoCrFeNiSi HEA is calculated to be -47.67 KJ/mol from Thermo-Calc (TC_HEA_3). The possible α phase to form during sintering are CrCoSi (-42.12 KJ/mol), CoNiSi (-48.06 KJ/mol), and (Co)2Si (-43.44 KJ/mol). EDS of 0Ni sample shows a slightly higher Si presence in the Cr rich region (2), which increases the possibility of CrCoSi formation. XRD peaks of CrCoSi also match with the current results, concluding the formation of CrCoSi α phase. The addition of Ni curbs the formation of α phase and promotes sigma (σ) phase formation. Fe and Cr are more likely to form the sigma phase at elevated temperatures. Ni is well known FCC and sigma phase stabilizer [30]. Ni and Cr are less likely to form a compound with each other, but their affinity towards Si may lead to precipitation of some ternary phase. Presence of fine black colored lamellas (4) in the Cr-rich region (2)

was found in 5Ni and 10Ni samples. The higher affinity of Si towards Ni can be observed from the EDS (region (4)) of Ni containing alloys. The compound of higher Si content is observed on the Cr rich region in 0Ni sample (region (2)), whereas same was observed in Ni-rich region in 5Ni and 10Ni samples. Small-sized precipitates (2, B and C) could be sharp edged σ phase. σ phase is more likely a Fe-Cr-Ni rich phase, which gets stable upon further Ni addition and can also be correlated with XRD results.

Ni additive has modified the microstructures of the alloys, as mentioned above. It has been highly beneficial in improving the mechanical properties. It improved the hardness of the base alloy. The compressive strength of the alloys was enhanced by about ~72%, while plastic strain was also doubled before fracture. It is obvious that Ni has promoted binding of the grains and ductility. It could also be attributed to the formation of fine lamina and fine rod-shaped precipitates in the sample.

5. Conclusions

BCC rich AlCoCrFeNiSi HEA powder was synthesized by mechanical alloying. Additional amount of nickel powder was added during sintering stage and hot pressed. Ni has modified the microstructure significantly, with increased amount of fine precipitates and fibers. This has led to increase the hardness and strength. Ultra-high compressive strength of about 3.04 GPa was achieved with considerable strain, by Ni addition. The result of this investigation is highly encouraging, and further study to achieve full density and to push the strength and ductility further higher, will continue.

6. References:

- [1] D. B. Miracle and O. N. Senkov, "A critical review of high entropy alloys and related concepts," *Acta Mater.*, vol. 122, pp. 448–511, 2017, doi: 10.1016/j.actamat.2016.08.081.

Table 1 Negative Enthalpy of formation among Al, Co, Cr, Fe, Ni, Si.

Elements	Al	Co	Cr	Fe	Ni	Si
Al	0	-19	-10	-11	-22	-2
Co	B2	0	-4	-1	0	-21
Cr	Complex	HCP	0	-1	-7	-20
Fe	B2	B2	BCC	0	-2	-18
Ni	B2	FCC	BCC	FCC	0	-23
Si	Diamond, FCC_Al	Alpha	Diamond, Alpha	B2, Diamond,	FCC	0

IMPROVEMENT OF MECHANICAL PROPERTIES OF AlCoCrFeNiSi HIGH ENTROPY ALLOY BY Ni ADDITIVE SINTERING

- [2] B. S. Murty, J. W. Yeh, S. Ranganathan, and P. P. Bhattacharjee, "Physical metallurgy of high-entropy alloys," in *High-Entropy Alloys*, Elsevier, 2019, pp. 31–50.
- [3] M. C. Gao, P. K. Liaw, J. W. Yeh, and Y. Zhang, *High-entropy alloys: Fundamentals and applications*. 2016, cham: Springer International Publishing.
- [4] D. B. Miracle, J. D. Miller, O. N. Senkov, C. Woodward, M. D. Uchic, and J. Tiley, "Exploration and development of high entropy alloys for structural applications," *Entropy*, vol. 16, no. 1, pp. 494–525, 2014, doi: 10.3390/e16010494.
- [5] B. Cantor, I. T. H. Chang, P. Knight, and A. J. B. Vincent, "Microstructural development in equiatomic multicomponent alloys," *Mater. Sci. Eng. A*, vol. 375–377, no. 1-2 SPEC. ISS., pp. 213–218, 2004, doi: 10.1016/j.msea.2003.10.257.
- [6] J. W. Yeh, S-K. Chen, S-J. Lin, J-Y. Gan, T-S. Chin, T-T. Shun, C-H. Tsau, and S-Y. Chang., "Nanostructured high-entropy alloys with multiple principal elements: Novel alloy design concepts and outcomes," *Adv. Eng. Mater.*, vol. 6, no. 5, pp. 299–303, 2004, doi: 10.1002/adem.200300567.
- [7] S. Ranganathan, "Alloyed pleasures: Multimetallc cocktails," *Curr. Sci.*, vol. 85, no. 10, pp. 1404–1406, 2003.
- [8] E. P. George, W. A. Curtin, and C. C. Tasan, "High entropy alloys: A focused review of mechanical properties and deformation mechanisms," *Acta Mater.*, vol. 188, pp. 435–474, 2020, doi: 10.1016/j.actamat.2019.12.015.
- [9] B. S. Murty, J. W. Yeh, S. Ranganathan, and P. P. Bhattacharjee, "Alloy design and phase selection rules in high-entropy alloys," *High-Entropy Alloy.*, vol. 4, no. 1953, pp. 51–79, 2019, doi: 10.1016/b978-0-12-816067-1.00004-7.
- [10] K. K. Alaneme, M. O. Bodunrin, and S. R. Oke, "Processing, alloy composition and phase transition effect on the mechanical and corrosion properties of high entropy alloys: A review," *J. Mater. Res. Technol.*, vol. 5, no. 4, pp. 384–393, 2016, doi: 10.1016/j.jmrt.2016.03.004.
- [11] C. Chattopadhyay, A. Prasad, and B. S. Murty, "Phase prediction in high entropy alloys – A kinetic approach," *Acta Mater.*, vol. 153, pp. 214–225, 2018, doi: 10.1016/j.actamat.2018.05.002.
- [12] Q. Wu, Z. Wang, F. He, J. Li, and J. Wang, "Revealing the Selection of σ and μ Phases in CoCrFeNiMox High Entropy Alloys by CALPHAD," *J. Phase Equilibria Diffus.*, vol. 39, no. 4, pp. 446–453, 2018, doi: 10.1007/s11669-018-0659-7.
- [13] A. M. Manzoni and U. Glatzel, "New multiphase compositionally complex alloys driven by the high entropy alloy approach," *Mater. Charact.*, vol. 147, no. June, pp. 512–532, 2019, doi: 10.1016/j.matchar.2018.06.036.
- [14] X. Chang, M. Zeng, K. Liu, and L. Fu, "Phase Engineering of High-Entropy Alloys," *Adv. Mater.*, vol. 32, no. 14, pp. 1–22, 2020, doi: 10.1002/adma.201907226.
- [15] M. Vaidya, A. Prasad, A. Parakh, and B. S. Murty, "Influence of sequence of elemental addition on phase evolution in nanocrystalline AlCoCrFeNi: Novel approach to alloy synthesis using mechanical alloying," *Mater. Des.*, vol. 126, no. January, pp. 37–46, 2017, doi: 10.1016/j.matdes.2017.04.027.
- [16] S. Rohila, R. B. Mane, G. Ummethala, and B. B. Panigrahi, "Nearly full-density pressureless sintering of AlCoCrFeNi-based high-entropy alloy powders," *J. Mater. Res.*, vol. 34, no. 5, pp. 777–786, 2019, doi: 10.1557/jmr.2019.9.
- [17] K. Jeong, J. E. Jin, Y. S. Jung, S. Kang, and Y. K. Lee, "The effects of Si on the mechanical twinning and strain hardening of Fe-18Mn-0.6C twinning-induced plasticity steel," *Acta Mater.*, vol. 61, no. 9, pp. 3399–3410, 2013, doi: 10.1016/j.actamat.2013.02.031.
- [18] D. Li and Y. Zhang, "The ultrahigh charpy impact toughness of forged AlxCoCrFeNi high entropy alloys at room and cryogenic temperatures," *Intermetallics*, vol. 70, pp. 24–28, 2016, doi: 10.1016/j.intermet.2015.11.002.

IMPROVEMENT OF MECHANICAL PROPERTIES OF AlCoCrFeNiSi HIGH ENTROPY ALLOY BY Ni ADDITIVE SINTERING

- [19] A. K. Gupta, D. J. Lloyd, and S. A. Court, "Precipitation hardening in Al-Mg-Si alloys with and without excess Si," *Mater. Sci. Eng. A*, vol. 316, no. 1-2, pp. 11-17, 2001, doi: 10.1016/S0921-5093(01)01247-3.
- [20] S. Rohila, R. B. Mane, S. Naskar, and B. B. Panigrahi, "Viscous flow assisted sintering of AlCoCrFeNi high entropy alloy powder," *Mater. Lett.*, vol. 256, no.126668, 2019, doi: 10.1016/j.matlet.2019.126668.
- [21] J. M. Zhu, H. M. Fu, H. F. Zhang, A. M. Wang, H. Li, and Z. Q. Hu, "Synthesis and properties of multiprincipal component AlCoCrFeNiSix alloys," *Mater. Sci. Eng. A*, vol. 527, no. 27-28, pp. 7210-7214, 2010, doi: 10.1016/j.msea.2010.07.049.
- [22] G. Zhang, H. Liu, X. Tian, P. Chen, H. Yang, and J. Hao, "Microstructure and Properties of AlCoCrFeNiSi High-Entropy Alloy Coating on AISI 304 Stainless Steel by Laser Cladding," *J. Mater. Eng. Perform.*, vol. 29, no. 1, pp. 278-288, 2020, doi: 10.1007/s11665-020-04586-3.
- [23] S. Gorsse, M. H. Nguyen, O. N. Senkov, and D. B. Miracle, "Database on the mechanical properties of high entropy alloys and complex concentrated alloys," *Data Br.*, vol. 21, pp. 2664-2678, 2018, doi: 10.1016/j.dib.2018.11.111.
- [24] L. Tian, M. Fu, and W. Xiong, "Microstructural evolution of AlCoCrFeNiSi high-entropy alloy powder during mechanical alloying and its coating performance," *Materials (Basel)*, vol. 11, no. 2, 2018, doi: 10.3390/ma11020320.
- [25] C. Xiang, Z. M. Zhang, H. M. Fu, E. H. Han, H. F. Zhang, and J. Q. Wang, "Microstructure and corrosion behavior of AlCoCrFeNiSi0.1 high-entropy alloy," *Intermetallics*, vol. 114, no. 106599, 2019, doi: 10.1016/j.intermet.2019.106599.
- [26] A. Kumar, A. K. Swarnakar, and M. Chopkar, "Phase Evolution and Mechanical Properties of AlCoCrFeNiSix High-Entropy Alloys Synthesized by Mechanical Alloying and Spark Plasma Sintering," *J. Mater. Eng. Perform.*, vol. 27, no. 7, pp. 3304-3314, 2018, doi: 10.1007/s11665-018-3409-4.
- [27] B. S. Murty, J. W. Yeh, S. Ranganathan, and P. P. Bhattacharjee, "Solid solution phases and their microstructures in HEAs," *High-Entropy Alloy*, Elsevier, pp. 119-144, 2019.
- [28] J. M. Zhu, H. M. Fu, H. F. Zhang, A. M. Wang, H. Li, and Z. Q. Hu, "Synthesis and properties of multiprincipal component AlCoCrFeNiSix alloys," *Mater. Sci. Eng. A*, vol. 527, no. 27-28, pp. 7210-7214, 2010, doi: 10.1016/j.msea.2010.07.049.
- [29] B. Jin, N. Zhang, F. Wang, Y. Zhang, and D. Li, "Phase evolution and wear mechanism of AlCoCrFeNiSix high-entropy alloys produced by arc melting," *Mater. Res. Express*, vol. 5, no. 9, p. 096505, Aug. 2018, doi: 10.1088/2053-1591/aad52b.
- [30] S. A. Kube, S. Sohn, D. Uhl, A. Datye, A. Mehta, and J. Schroers, "Phase selection motifs in High Entropy Alloys revealed through combinatorial methods: Large atomic size difference favors BCC over FCC," *Acta Mater.*, vol. 166, pp. 677-686 2019, doi: 10.1016/j.actamat.2019.01.023.

SINTERING CONDITIONS AND MECHANICAL PERFORMANCES OF LOW NICKEL PM CHROMIUM STEELS

Ivan Lorenzon, Franco Buzzelli, Mirko Nassuato

Pometon S.p.A., Italy

Abstract: *The ongoing volatility of the commodities market and the tightening of chemical risk legislation are making the extra performance of highly alloyed materials increasingly more expensive, at a time when qualitative requirements on sintered components keeps rising. Driven by economical and environmental issues, the formulation of the powders used in this presentation is based on optimising the chemical composition for achieving the best performance of these sinter-hardening PM steels with a minimum of alloying elements. In this presentation, a family of high strength and cost effective PM steels, developed by mixing selected combinations of alloying elements in different and predetermined concentrations will be shown. One of the main purposes has been achieving an optimum balance between compressibility, hardenability and other sintering properties in relation with the mechanical properties (hardness, toughness and fatigue). The basic PM steel, called ECOSint A, can be adjusted through further alloying additions of chromium, nickel (<1%wt) and copper (<1%wt). Given a certain set of sintering conditions, final properties can be tailored to fit the designed requirements, in terms of dimensional change, microstructure and mechanical properties. Sizeable to fully sinter-hardened steel grades can be obtained with standard sintering furnaces and cooling rates. However, by using high oxygen affinity elements as alloying additions a more stringent control of the sintering conditions, as well as, low oxygen starting powders are generally required. In this presentation some suggestions about thermal treatment conditions and sintering atmospheres will be introduced.*

Introduction

Alloy design based on a proper selection of alloying elements combined with an adequate alloying method can also be aimed at obtaining more economical processing for instance by sinter-hardening. The requirement of high performance materials under dynamic loading in service makes fatigue resistance one of the most important properties. In the present work the mechanical properties of PM steels obtained from recently developed Cr-containing powders were studied with the main objective to evaluate fatigue resistance. However, other mechanical characteristics such as UTS, elongation, impact energy and hardness, obtained from the same batch of powders and sintered under identical conditions, are also reported. Since 3-point bending fatigue is not a commonly used testing method a set of samples prepared from other

commercially available powders was used for comparison purposes. A suggested explanation on the test results is described.

In this document a combined experience sintering Cr-containing PM steel ECOSINT A in endogas and Hydrogen/Nitrogen atmospheres at 1120°C is summarised. The work also presents an analysis of the effect of sintering atmospheres on the oxide reduction during sintering with experimental illustration using Ecosint+graphite powder compacts. The experimental results discuss the difference in terms of hardness and Chromium oxide formation between endogas and Hydrogen/Nitrogen atmospheres.

Experimental Procedure

PM steels used in this work were prepared from the newly developed chromium-containing Fe based ECOSint powder family. Table 1 shows

SINTERING CONDITIONS AND MECHANICAL PERFORMANCES OF LOW NICKEL PM CHROMIUM STEELS

the nominal chemical composition of the PM steels identified as different alloys from A to D. As seen from the Table, and without considering graphite, the total amount of alloying elements in these PM steels is between 2.6 and 4.2 in weight percent.

The fatigue properties for these PM steels were evaluated using 3- point bending fatigue testing with bar shape (TRS) specimens (31.7x12.7x6.35 mm) applying MPIF Standard 41 (figure 1).

Table 1: ECOSINT Series- composition

Alloying elements (%)	ECOSINT A	ECOSINT B	ECOSINT C	ECOSINT D
Ni	0.4	0.9	0.9	0.4
Mo	0.8	0.8	0.8	0.8
Fe	Balance	Balance	Balance	Balance
Cr	1.4	1.4	1.4	1.4
Cu	-	-	1	1
Total Alloying	2.6	3.2	4.2	3.6

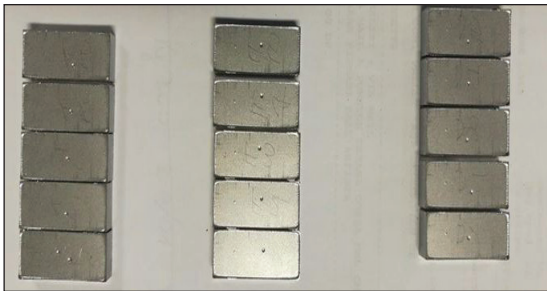


Fig. 1: TRS bar shape samples

ECOSint powders (table 1) were mixed with additional graphite and die pressed at 750 MPa reaching a density between 7.0 and 7.1g/cm³. Sixty specimens per material were cold pressed in order to use 15 specimens for producing each S-N curve. Specimens were sintered at 1120°C and 1240°C for 30 min followed by normal (0.25°C/s) or accelerated cooling (~1°C/s). After sintering all the specimens were subjected to a stress relief treatment at 200°C for 1hr. Sintering and tempering were carried out using a 90N2-9H2-1CH4 atmosphere. Final densities were measured by the Archimedes principle on selected TRS specimens.

Before testing all specimen corners were lightly polished in the longitudinal direction using emery paper to eliminate asperities. The fatigue tests were performed at room temperature with a load factor of R = 0.1 and calculations were carried out based on the following equations:

$$P = \frac{3}{2} * \frac{\sigma_{max}}{b * h} * \frac{L}{h} * (1 - R)$$

Where,

L: 25.4 mm

R: 0.1

σ_{max} : Load applied [N]

b: Width [mm]

h: Thickness [mm]

Yielding:

$$P = 34.29 * \frac{\sigma_{max}}{b * h^2}$$

It is important to emphasize that due to the reduced number of specimens tested (15 specimens per SN curve) the reported data should be taken with caution. Nevertheless, it must also be pointed out that in all cases five run-outs were invariably imposed to determine the fatigue strength. The criterion fixed for a run-out was a survival >107 cycles without fracture. Finally, some specimens were used for preparing polished cross sections to be observed under the optical microscope and measure apparent hardness.

In this document, for Ecosint A, the differences in terms of metallographic phases between Endogas and Hydrogen/Nitrogen/Methane sintering at 1120°C are showed. Differences in terms of “dew point” lead to differences in mechanical properties due to the formation of unwanted phases.

Results and Discussion

Mechanical properties of Ecosint series by LTS and HTS

Figures 2 and 3 show the S-N curves corresponding to the PM steels while Figure 4

SINTERING CONDITIONS AND MECHANICAL PERFORMANCES OF LOW NICKEL PM CHROMIUM STEELS

shows summary of the data including results obtained after high temperature sintering. For identification the figures also show the sintering conditions and cooling rates used as well as the measured density and carbon in solution prior to testing. As a nomenclature in the Figures, sintering temperatures of 1120 and 1240°C are identified by LTS and HTS respectively, while cooling rates of 0.25 and 0.88°C/s are indicated as NC and RC. It may be seen that Alloy A sintered at 1120°C and cooled normally (0.25°C/s) shows fatigue strength of 340 MPa at the same time that increasing Ni (Alloy B) produces an increase of fatigue strength to 375MPa. Nevertheless, a drop in fatigue resistance is observed for Alloy D which seems to be associated to adding Cu without increasing Ni.

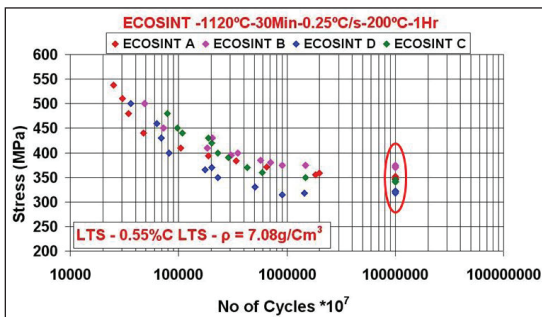


Fig. 2 : 3-point bending fatigue results for Alloys A, B, C, and D sintered at 1120°C for 30min followed by cooling at 0.25°C/s and tempered at 200°C for 1hr. Run-outs encircled

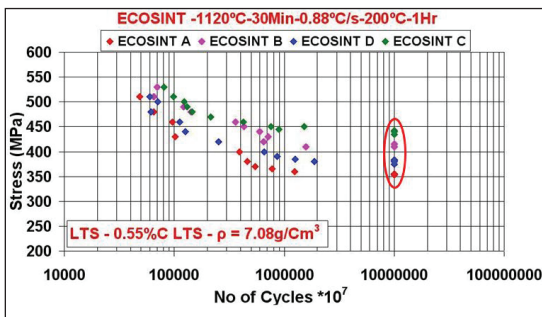


Fig. 3 : 3-point bending fatigue results for Alloys A, B, C, and D sintered at 1120°C for 30min followed by cooling at 0.88°C/s and tempered at 200°C for 1hr. Run-outs encircled.

As noticed in Figure 4, Alloy D gives the lowest fatigue strength of all material in this group independently of the sintering temperature and cooling rate used. That additional Ni has a positive effect on fatigue strength is supported by the response observed from other mechanical properties obtained in this work. Table 2 includes data like UTS, elongation and fractures toughness. Clearly, an increase in fatigue strength is produced as the Ni content is also increased. Alloy C which also contains copper seems to benefit particularly from an accelerated cooling rate (Figure 2). In this case, combining an accelerated cooling rate around 0.9°C/s with conventional sintering temperature results in a fatigue strength of 440 MPa.

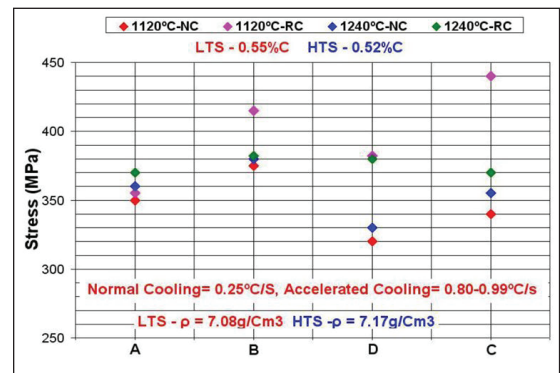


Fig. 4: Fatigue results for Alloys A, B, C, and D after 3-point bending fatigue testing.

Figure 4 also shows high temperature sintering results in a slight increase in density for all the specimens thus reaching an average value around 7.17g/cm³. Fatigue results after HTS-NC show nearly the same trend observed with LTS-NC since Ni seems to favour higher fatigue strength. It may also be noticed that despite the increase in density HTS shows only a marginal change in fatigue properties. The fatigue results obtained after HTS followed by normal cooling are in the range of 350- 380MPa. A slight increase is also observed after accelerated cooling, however, such an increase is not as pronounced as that obtained after LTS. According to the data

SINTERING CONDITIONS AND MECHANICAL PERFORMANCES OF LOW NICKEL PM CHROMIUM STEELS

Table 2: Summary of mechanical properties for alloys A, B, C and D after different combinations of sintering conditions and cooling rates.

Material	Chemical comp. (Wt %)	Sintering Cond.	cooling rate (°C/s)	UTS (MPa)	E. (%)	3 point bending Endurance limit (MPa)	I. energy (J)	Apparent Hardness HV30
Ecosint A	1.4Cr-0.8Mo-0.4Ni	1120°C-30min	0.25	708	1.58	350	12	173
Ecosint B	1.4Cr-0.8Mo-0.9Ni			787	1.6	375	15	196
Ecosint C	1.4Cr-0.8Mo-0.9Ni-1Cu			772	1.44	340	12	230
Ecosint D	1.4Cr-0.8Mo-0.4Ni-1Cu			759	1.62	320	14	248
Ecosint A	1.4Cr-0.8Mo-0.4Ni	1240°C-30min		867	2.44	360	24	196
Ecosint B	1.4Cr-0.8Mo-0.9Ni			844	2.05	380	25	234
Ecosint C	1.4Cr-0.8Mo-0.9Ni-1Cu			905	2.22	355	22	230
Ecosint D	1.4Cr-0.8Mo-0.4Ni-1Cu			926	1.99	330	22	286
Ecosint A	1.4Cr-0.8Mo-0.4Ni	1120°C-30min	0.8-1	848	1.2	355	15	230
Ecosint B	1.4Cr-0.8Mo-0.9Ni			1009	1.28	415	16	272
Ecosint C	1.4Cr-0.8Mo-0.9Ni-1Cu			932	1.16	440	15	279
Ecosint D	1.4Cr-0.8Mo-0.4Ni-1Cu			948	0.95	380	16	354
Ecosint A	1.4Cr-0.8Mo-0.4Ni	1240°C-30min		1105	1.2	370	20	254
Ecosint B	1.4Cr-0.8Mo-0.9Ni			1043	2.16	380	19	272
Ecosint C	1.4Cr-0.8Mo-0.9Ni-1Cu			1098	1.6	370	20	318
Ecosint D	1.4Cr-0.8Mo-0.4Ni-1Cu			1277	1.51	380	18	382

in Figure 4 nearly all values of fatigue strength are found in a range from 340-390MPa, whereas Alloys B and C stand out after LTS followed by accelerated cooling. This negligible influence of HTS is not well understood yet so that further research is underway. On the other hand, as realized from Table 2, an important benefit is obtained after HTS in terms of increased elongation and impact energy.

This effect is expectedly less pronounced as the amount of alloying elements is increased since higher hardness and mechanical strength are simultaneously obtained. The important influence exerted by accelerated cooling after LTS is clearly associated with a noticeable increase in the amount of martensite formed.

Considering the properties reported in Table 2, it may be realized that after HTS and normal cooling the material also develops a high amount of martensite but reaches lower hardness and UTS values than those attained by combining 1120°C with accelerated cooling. It must also

be pointed out that increasing the cooling rate after HTS, thus obviously increasing the amount of martensite, produces higher hardness, UTS, elongation and impact energy but, as mentioned before, a surprisingly lower fatigue resistance.

The study of the connection between carbon content/heat treatments and mechanical properties/metallographic phases is underway in a European project.

As mentioned before the fatigue results obtained for these alloys were compared against those obtained under exactly the same fatigue testing conditions but using some well known commercially available PM powders. The mechanical properties for these commercial alloys are included in Table 3. For a comparative evaluation it may be realised that the fatigue resistance obtained for these PM steels is higher or at least comparable to that of the commercially available alloys. The higher amount of alloying elements contained in those PM steels does not seem to give extra benefits as compared to those presented here. It may be pointed out that the hybrid with 1.5 % Mo (4%Ni) reaches 363 MPa bending fatigue strength after HTS whereas the specimen from Alloy B reaches 380MPa fatigue strength after sintering at 1120°C and followed by normal cooling. It is important to emphasize that this latter PM steel only contains 0,9%Ni. The prealloyed Cr steel shows a benefit on fatigue strength from HTS that the alloys presented here do not seem to exhibit. It is however interesting to notice that Alloy C does not seem to require HTS since after 1120°C followed by accelerated cooling (< 1°C/s) the PM steel develops 440 MPa fatigue strength.

Table 3: Mechanical properties, sintering parameters and fatigue results of well known commercial steels after 3-point bending fatigue in the as-tempered condition.

Material	Alloy content (Wt %)	Sinter T [°C]	CR [°C/s]	%C Real	Dens [g/cm ³]	%E	UTS [MPa]	Three point Bending Fatigue [MPa]
Cr-Prealloyed	3.5	1120	0.45	0.41	7.03	1.08	799	395
Cr-Prealloyed	3.5	1240		0.28	7.17	1.99	922	429
Hybrid1.5%Mo	7.41	1240		0.59	7.23	2.5	1080	363

SINTERING CONDITIONS AND MECHANICAL PERFORMANCES OF LOW NICKEL PM CHROMIUM STEELS

Influence of the sintering atmosphere on metallographic phases

Two trials of sintering, reported in the following table 4, were performed to understand the influence of atmosphere in the sintered part. In this test Dew point values are measured by gas sampling inside the hot zone. Also in this case the geometry of the sintered part is the TRS bar described before.

Table 4: Sintering conditions

Test [N°]	Material	Furnace	Sintering T [°C]	Sintering Atmosphere	Time in Hot zone	Dew point [°C]
1	Ecosint A + 0,6% C + 0,8% Lube	Continuous Furnace	1120	Endogas methane/air 1/1,8 ratio	30 minute	-17
2	Ecosint A + 0,6% C + 0,8% Lube	Continuous Furnace	1120	N ₂ 76%, H ₂ 20%, CH ₄ 4%	30 minute	-54

After sintering, measurements of Archimede density, microhardness and macrohardness were carried out to analyze the physical differences between the two tests which differ only in the atmosphere of sintering. The differences are reported in the table 5 below.

Table 5: Archimede density, microhardness and macrohardness of test 1 and test 2

Test [N°]	Archimede Density	Micro hardness [200g]	Apparent hardness [HV30]
1	6,93	307	144
2	6,98	298	310

In table 5, micro and apparent hardness are reported. It is evident that the hardness of the single particles is very similar between test 1 and test 2 but the apparent hardness is completely different.

To study this effect several, SEM analysis, elemental maps and EDS have been performed.

Fig. 5, 6 & 7 shows that there are differences between the interparticle connections between test 1 and test 2.

Test 1 in fact shows the interparticle detachments that can explain the mechanical differences in terms of apparent hardness and micro hardness.

For this reason, further analyses have been performed by electron microscope.

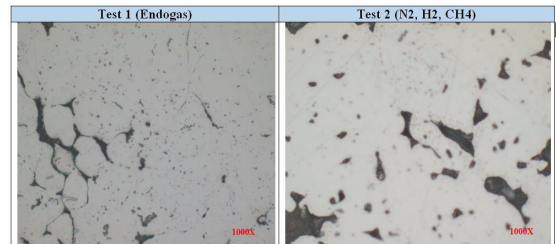


Fig 5: optical analysis of sintered part produced in Test 1 and Test 2

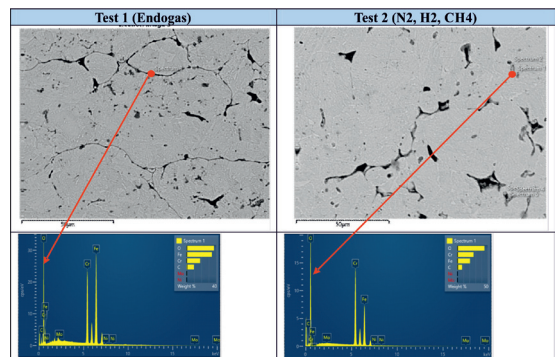


Fig 6: electron backscatter and EDS analysis on sintered parts

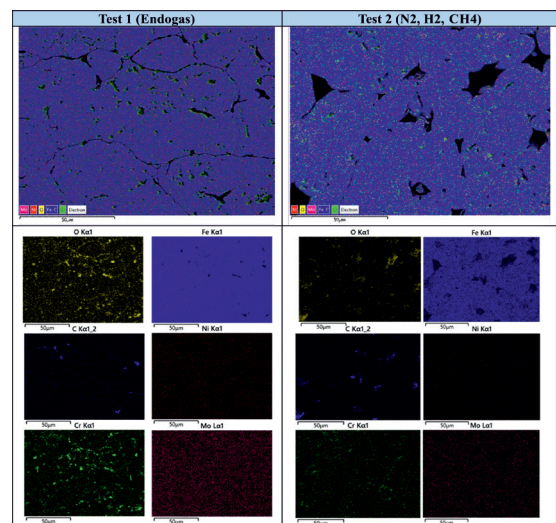


Fig 7: elemental mapping on sintered parts

SINTERING CONDITIONS AND MECHANICAL PERFORMANCES OF LOW NICKEL PM CHROMIUM STEELS

By electron backscatter and EDS analysis, it is possible to evaluate the interparticle discontinuity in test 1 (Endogas) due to the formation of Chromium/Iron Oxides.

In test 2 it is also possible to find oxides but inside the metal matrix (not in the particle surface).

Also the elemental mapping in Fig. 7 supports the hypothesis that the formation of oxides, around the sintered particles, compromises the mechanical properties of iron chromium alloy.

Conclusion

The alloyed powders hereby developed allow us to obtain high performance steels of the sinter-hardening type which exhibit interesting properties for highly demanding applications. It is demonstrated that the sinterhardening characteristics may be tuned with ease by selecting adequate combinations of chemical composition, sintering temperature and cooling rate. Using an accelerated cooling rate $<1^{\circ}\text{C/s}$ is beneficial for obtaining high fatigue strength.

Besides, the sinter-hardening response of some of these steel grades allows to obtain components with high amounts of martensite at very conservative cooling rates. Increased nickel contents helps achieving better mechanical properties, especially fatigue strength. In contrast copper-additions produce an increase of UTS and hardness but cause a drop of fatigue properties. Additionally, the evaluation of other commercially available grades using the same fatigue test method proves that fatigue strength of ECOsint grades are comparable to other well known commercial powders.

The present study underlines the necessity for the sintering atmosphere to have a Dew point as low as possible, suggestible at least less than -30°C in order to avoid the formation of Cr oxides which otherwise would inhibit the interparticulate cohesion.

The use of an Endogas atmosphere is strongly not recommendable.

Reference

1. F. J. Esper and C. M. Sonsino, "Fatigue design for PM components", Published by EPMA, Shrewsbury, England, 1994.
2. P. Beiss and M. Dalgic, "Structure property relationships in porous sintered steels", *Materials Chemistry and Physics*, 2001, vol. 67, N° 1-3, 37-42.
3. P. Beiss, "Functional relationships between fatigue data", *Materials Science Forum*, 2007, 534-536, 681-684.
4. H. Danninger and B. Weiss, "The influence of defect on high cycle fatigue of metallic materials", *J. of Mat. Processing Technol.*, 2003, vol 143-144, 179-184.
5. S. Saccarola, S. Sainz, A. Karuppanagounder, F. Castro, "Hardenability and mechanical properties of novel sinterhardening PM steels", *Adv. in Powder Met & Part Mater* 10, 52 (2009).
6. S. Saccarola, G. Bellin, S. Bueno, S. Sainz and F. Castro, "Novel high performance and dimensionally controlled PM steels for sinterhardening", *Euro PM2009, Sintered Steels III, Copenhagen, Denmark* (2009).
7. S. Saccarola, A. Karuppanagounder, S. Sainz and F. Castro, "Developing novel Cr-Mo-Ni PM steels", *PM World Congress and Exhibition*, (2010), Florence, Italy.
8. I. Rampin, M. Zanon, S. Saccarola and F. Castro, "Influence of Selected Alloying Elements on the Hardenability and Fatigue Strength of Recently Developed Sinter-Hardening PM Steels", *Euro PM2011, Barcellona* (2011)

MICROSTRUCTURAL CHARACTERIZATION OF AlCoNiVWC HIGH ENTROPY ALLOY CLADDING ON IS2062 STEEL

A. Verma, M. Abhinav, Shanmugasundaram T.*

Department of Metallurgical and Materials Engineering, Defence Institute of Advanced Technology, Pune, India

Abstract: High entropy alloys (HEA), also called multiple principal element alloy, consist of five or more than five principal components mixed in equiatomic or non-equiatomic ratios. HEA material shows high toughness, high-temperature strength, excellent creep, wear, and corrosion resistance because of following four core effect which includes high entropy effect, large lattice distortion, slow diffusion, and cocktail effect. AlCoNiVWC high-entropy alloy (HEA) coating was applied on IS2062 steel plates by GTAW process to enhance surface properties. HEA powder was prepared by planetary ball mill for 30 hours. Samples were characterized by using scanning electron microscopy, microhardness, and wear testing machine. Micrograph results showed that the HEA coatings exhibited good metallurgical bonding to the substrate. HEA coating shows dilution till 3 mm from the surface with lathe type of features formed on the cladding surface while the substrate micrograph shows uniform grains size. Hardness of the steel increased from 158 HV to 338 HV after cladding and the wear properties increased by 20 times in comparison to the substrate.

Introduction:

Conventional alloys have been a field of research for a very long time. They have helped us make our life easier in ways that can't be explained in words. Conventional alloys are alloys that have one primary element, and other elements are added to it for enhancing its properties but retaining the original property of the primary element. Metallic bonding character is what defines an alloy ^[1,2]. In 2004 two publications independent of each other by Brian Cantor (UK) and Jein-Wei Yeh (Taiwan) opened the new doorway to the new alloy world. This led to future research in the new category of materials known as Multi-Principal-Element Alloys or High Entropy Alloys. High Entropy Alloys can be defined as the alloys having a minimum of 5 primary elements having atomic percentages between 5% to 35%. Any element with an atomic percentage of less than 5% is considered a minor element. Another definition is alloying with configurational entropy of more than 1.5 R, where R is the universal gas constant ^[3,4]. Combining with the effect of high entropy, lattice distortion, sluggish diffusion, and cocktail effect, HEAs have been reported to possess outstanding physical and mechanical properties,

such as good thermal stability, high hardness and strength, good ductility, excellent wear, and corrosion resistance, thus HEAs and related composites have great potentials in engineering applications ^[4-11].

In metals, cladding is usually done to improve the corrosion and wear resistance of the low-cost materials. HEAs with superior properties can be easily used for the surface modification of conventional alloy systems. Over the years, research have been done on coating mechanisms as the coating of metal with superior properties helps in increasing a variety of different properties like high hardness, provide thermal stabilities, and in case of the tool they prolong the life, thus helping in cost-effective production. HEA's have been coated using various fabrication techniques, which include thermal spraying, gas tungsten arc welding (GTAW), laser cladding, and sputtering. Small thickness and rapid solidification associated with these techniques induces higher cooling rate on the coating. Moreover, due to sluggish diffusion at higher cooling rates reduces coarsening of grains which in turn increase the strength or hardness of the cladding ^[5].

MICROSTRUCTURAL CHARACTERIZATION OF AlCoNiVWC HIGH ENTROPY ALLOY CLADDING ON IS2062 STEEL

Shen et al., have developed $(Al_{0.34}Cr_{0.22}Nb_{0.11}Si_{0.11}Ti_{0.22})_{50}N_{50}$ high-entropy nitride coatings on WC/Co substrates by reactive magnetron sputtering and compared the results with the conventionally coated TiN and TiAlN. The results showed that HEA nitride coating has better thermal stability, outstanding oxidation resistance and high hardness than the substrate material^[12]. Juan Xu et al. coated Q235 Steel with CoCrFeNi high-entropy alloy having different weight ratios of WC, i.e., 10% and 30%. The thickness obtained after the coating was 860 μm and 900 μm for 10% and 30% WC HEA carbide, respectively. Microhardness of the coating was 475 and 531 HV for 10 and 30% WC HEA carbide, respectively. These values are approximately three times that of the substrate hardness, which is around 160 HV. The hardness increment was attributed to two reasons; one with an increase in W content, and other with grain refinement^[13]. In another study, (TiVCrZrHf)N multi-component alloy system was deposited by reactive magnetron sputtering system to study the structure, mechanical properties, and composition of the coating deposited at different Nitrogen flow rates. The maximum hardness of 23.8 \pm 0.8 GPa was observed due to the formation of nitrides and moderate grain size^[14]. Coating of FeCoCrNiNbX ($x=0.25, 0.6$ & 0.8) HEA using plasma cladding on Titanium substrate showed dendritic microstructures with the main phase was FCC and a small amount of BCC phase. As the content of Nb increased, so did the BCC phase, which increases the hardness of HEA coating and Nb_{0.6} recorded the highest hardness of 598 HV with the highest wear resistance^[15].

$Al_2CrFeNiCoCuTi_x$ ($X=0.0, 0.5, 1.0, 1.5$ & 2.0) was coated on Q235 steel substrate by laser cladding. $Ti_{0.0}$ shows FCC structure while $Ti_{0.5}$ contained Laves phase + BCC1 + BCC2 + FCC, which have high hardness due to BCC and Laves phase. In $Ti_{1.0}$, Laves phase was close to 0, so its wear resistance is less than $Ti_{0.5}$ alloy, while $Ti_{2.0}$ alloy coating had BCC as a single

structure but relatively low hardness, so the relative wear resistance was the lowest^[16]. AlCoCrFeNiTi High-Entropy Alloy Coating was prepared on 316 stainless steel substrates with the help of a high-energy atmospheric plasma-spraying system which shows microhardness of 710 HV^[17]. NiCrAlCoW and NiCrAlCoSi were coated on AISI 1050 medium carbon steel by the process of TIG cladding. When the hardness was compared, the alloy with W had higher hardness than the alloy with Si, and the hardness of NiCrAlCoW was around 720 HV. The dense dendrite and the matrix had a strong bond because of the mechanical interlocking and the geometrical effect, which reduced the wear rate of the coating in the case of HEA with W. The mechanical interlocking in alloy with Si is less than the interlocking in an alloy containing W; thus, the wear rate of the latter is more compared to the former^[18]. NiCrAlCoCu and NiCrAlCoMo multicomponent alloy were synthesized on AISI 1050 medium carbon steel using the TIG cladding process. The hardness of the NiCrAlCoMo clad layer is more than that of the NiCrAlCoCu clad layer, approximately four times. A significant number of various intermetallic compounds are formed in the NiCrAlCoMo clad layer. Due to the formation of vein-shaped reinforcement in the NiCrAlCoMo clad layer, strong mechanical interlocking can be seen. This gives NiCrAlCoMo clad layer significantly better wear performance than NiCrAlCoCu clad layer^[19]. The above literature provides insight on HEA coating that can improve the hardness significantly, but very few works have been explored with HEA carbides; thus, in this work, HEA carbide coating was studied and explored. Here AlCoNiVWC cladding on IS 2062 substrate using GTAW process was prepared and analyzed for potential wear application.

Experimentation & procedure:

Al, Co, Ni, W, V metal powders and graphite powder with a purity of 99 percent were mixed in an equimolar ratio and were put in a planetary

MICROSTRUCTURAL CHARACTERIZATION OF AlCoNiVWC HIGH ENTROPY ALLOY CLADDING ON IS2062 STEEL

ball mill. The rpm was kept at 300, and the ball to powder ratio was held at 10:1 in weight. The ball mill was run for 20 hours. IS 2062 Steel substrate of 45x20x7 mm was cut using the cutting machine. One of the surfaces of the steel substrate was flattened using an emery paper of grade P120. The main aim was to create a rough surface for better adhesion of the coating. Then the surface was cleaned using acetone and was kept in an oven at 90°C for 4 hours. 2 g of HEA carbide powder was taken to coat over the prepared surface of steel substrate. PVA was used as the binder for the HEA carbide paste. The paste was applied over the prepared surface of the steel substrate using a flat spatula. The thickness of the paste was kept nearly at 1 mm. The ready sample was kept in an oven at 90°C overnight. The powder was held together with good binding by the PVA over the substrate, as shown in Fig.1.



Fig 1: Sample after the application of HEA Carbide blended with PVA.

Fronius MagicWave 3000 TIG welding machine was used to clad the HEA carbide over the substrate. The current was kept in a range of 85-90 A for each pass. A single-pass covered around 3-4 mm, and an overlapping of approximately 0.5 mm was observed. The torch speed was 100 mm/min. The sample after the cladding is shown in Fig. 2.



Fig 2: Sample after GTAW cladding

After cladding, the sample was cut across the cross-section of \varnothing 6 mm diameter and 15 mm length for wear testing, as shown in Fig. 3. Similarly, three \varnothing 6 mm diameter samples were cut from the IS 2062 steel substrate for comparison with 25 mm length

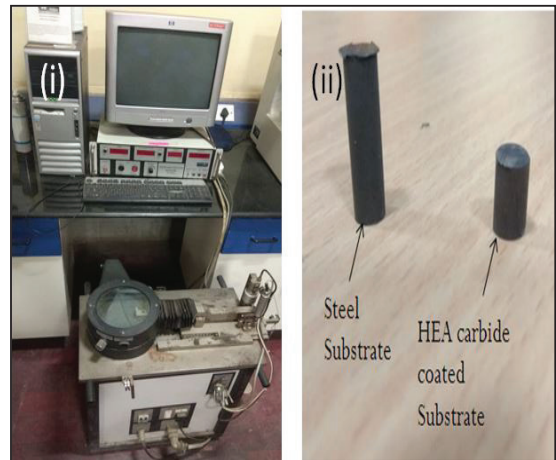


Fig 3: (i) Wear testing machine (ii) wear samples

The sample having the cross-section was prepared by using the polishing machine using emery paper of different grade sizes starting from 600 to 2000. Thereafter it was polished using diamond paste for mirror finishing. Microstructure of the samples at different regions was studied using a scanning electron microscopy (SEM). The hardness profile was

MICROSTRUCTURAL CHARACTERIZATION OF AlCoNiVWC HIGH ENTROPY ALLOY CLADDING ON IS2062 STEEL

taken using a MATSUZAWA MMT-X7 Vickers hardness testing machine at 0.3 kgf load and the dwell time of 10 s. The Figure 3a shows the DUCOM TR 20 series wear testing machine on which the dry wear testing of the samples (\varnothing 6 mm diameter) was done at room temperature, the sliding time was kept 30 min, and a distance of 1484 m was traveled at 315 RPM speed at 100 N load. Three samples of each uncoated and coated layer were tested, and the average wear rate was calculated.

Result & discussion:

Microstructure:

The SEM images were taken from different zones as shown in Fig. 4 (vii). The key observation made in the SEM micrographs is that the grain structure is changing from the lathe and dendritic to coarser grains as depth increases from the coating surface. The possible reason that can be cited for the change in the microstructure is the cooling rate and formation of HEA carbides at the surface. The cooling rate at the surface (zone 1) of the coating was very high, thus giving it refined grain structures, as shown in Fig. 4 (i). These lathe-type structures have a configuration similar to that of martensite in steel and exhibit similar properties, which will be discussed in a later section. The image in Fig. 4 (ii) represents zone 2, below zone 1 by 0.5 mm towards the base metal. In the Fig. 4(ii), we can see a coarser grain structure, and the amount of lathe has reduced due to the reduction of carbon because of dilution. Zone 3 of Fig. 4 (iii), which is further 0.5 mm deeper, has grain coarser than zone 2 due to slow dissipation of heat and lesser lathe structure due to further dilution. Fig. 4 (iv) is the image of zone 4 further 1.0 mm deeper than zone 3 and has a much coarser grain size, and the lathe structure has disappeared. Zone 5, shown in Fig. 4 (v), which is further 0.5 mm below zone 4, coarser grains are prominently observed. Zone 6, shown in fig. 4 (vi), is 0.5 mm below zone 5 and has the largest grain compared

to other zones, and is at the depth of 3 mm from the surface, shown in the schematic view of Fig. 4 (vii).

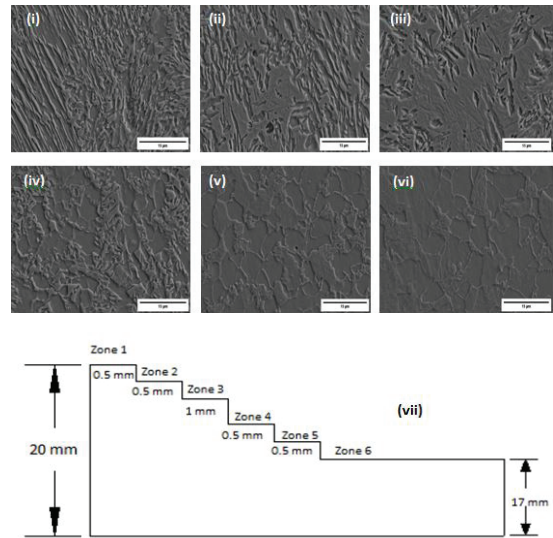


Fig. 4: SEM micrograph of different zones (i) Zone 1, (ii) Zone 2, (iii) Zone 3, (iv) Zone 4, (v) Zone 5, (vi) Zone 6 and (vii) Schematic view of different zones

Composition:

Table 1 depicts the elemental composition of different zones in weight percentage. It shows that there is the dilution of high entropy alloy into the substrate. This may be because of the high current used during the cladding process. The dilution was visible until 3 mm deep towards the base of the substrate. Elements like C, Al, V, Ni & W keep on decreasing in a different zone, and zone 6 has attained the composition of the substrate. Zone 1 has the highest amount of carbon and HEA elements. The lathe phases formed here could be the high entropy alloy carbides as they have a negative enthalpy of mixing and are most favored. As depth increases, it is observed that HEA elements decrease due to dilution, which in turn reduces the lathe type structure.

MICROSTRUCTURAL CHARACTERIZATION OF AlCoNiVWC HIGH ENTROPY ALLOY CLADDING ON IS2062 STEEL

Table 1: Elemental composition of the coated sample at different regions (zones)

Composition	C	Al	Si	V	Mn	Fe	Co	Ni	W
Zone 1	2.30	0.46	0.45	1.12	1.17	90.20	0.91	0.80	2.59
Zone 2	2.12	0.44	0.40	1.13	1.14	90.43	0.89	0.83	2.62
Zone 3	1.56	0.52	0.37	1.13	1.19	90.67	1.09	0.85	2.62
Zone 4	1.02	0.36	0.37	0.74	1.16	93.60	0.73	0.56	1.46
Zone 5	0.41	0.23	0.40	0.27	1.16	96.35	0.46	0.21	0.51
Zone 6	0.22	0.12	0.42	0.01	1.25	97.80	0.10	0.03	0.05

Hardness profile:

The hardness profile was taken across the cross-section of the sample. The graph shown in Fig. 5 shows the hardness profile obtained at a distance of 0.5 mm starting from the coating surface towards the bottom. As shown in the chart, coating hardness at the surface is 338 HV due to the formation of high entropy alloy carbides having lathe type structure and smaller grain size (Fig. 4 i). Further going down by 0.5 mm, there is a sudden decrease in the hardness value to 248 HV, and it steadily decreases till it reaches a value of 240 HV. The decrease in the hardness is because of the dilution of the high entropy alloy system into the substrate, as shown in table 1. There is a sudden decrease in the hardness at around 3.0 mm from the coating surface; the value reached 189 HV; this might be because it is a heat-affected zone (HAZ) and coarser grain size. Till 4.5 mm it can be observed

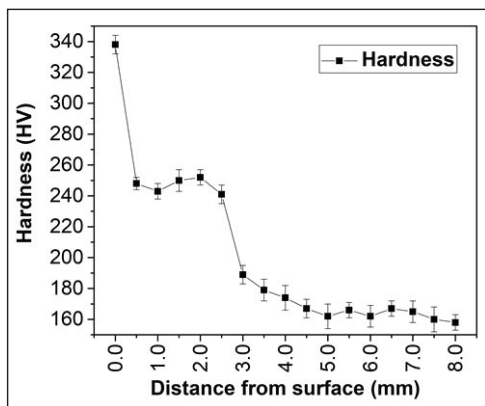


Fig. 5: Hardness profile of the coated sample at the cross-section.

that hardness kept on decreasing and attains a stable value below 5 mm from the surface, which can be called the limit of the HAZ region. The substrate, i.e., mild steel, has a hardness value in the range of 158-165 HV, as supported in the literature.

Wear results:

Three samples from the substrate material and the coated sample were tested, and the average value of the wear rate was measured, as shown in table 2

Table 2: Wear data for all the samples.

Sample Name	Weight before the test (g)	Weight after the test (g)	weight loss (g)	Sp. Wear rate ($\times 10^{-8}$ mm ³ /Nm)
S1	4.2041	4.1165	0.0876	4.7055
S2	4.2196	4.1493	0.0703	3.7762
S3	4.2619	4.2043	0.0576	3.8836
C1	1.8993	1.8960	0.0033	0.1779
C2	2.1313	2.1227	0.0086	0.2193
C3	1.9850	1.9812	0.0037	0.2019

The sample names S1, S2, and S3 represent the steel sample, and the samples C1, C2, and C3 represent the coated samples. From the above data, we can see that the specific wear resistance has undoubtedly increased drastically for the coated samples. The average wear rate is 4.1218×10^{-8} mm³/Nm for mild steel, and that of coated HEA was 0.1997×10^{-8} mm³/Nm. Thus, due to an increase in hardness by HEA carbide coating, it has been observed that the wear rate has decreased 20 times following Archard's law.

Conclusion:

- The AlCoNiVWC High Entropy Alloy Carbide coating was successfully developed on IS 2062 Mild Steel substrate using the GTAW cladding process.
- Dilution was observed up to 3 mm from the coated surface.
- The hardness measured at the top surface of the coating was around 338 HV, and that of the substrate was 158HV. This implies that the hardness was approximately doubled.

MICROSTRUCTURAL CHARACTERIZATION OF AlCoNiVWC HIGH ENTROPY ALLOY CLADDING ON IS2062 STEEL

- The wear rate of the steel after cladding has reduced approximately 20 times when compared to that of the mild steel substrate.

Reference:

1. Callister, W.D. "Materials Science and Engineering: An Introduction" 2007, 7th edition, John Wiley and Sons, Inc. New York, Section 4.3 and Chapter 9.
2. Smith CS (1963) Four outstanding researchers in metallurgical history. American Society from Testing and Materials, Baltimore.
3. Yeh J. Alloy Design Strategies and Future Trends in High-Entropy Alloys. JOM 2013;65:1759–71.
4. Michael C. Gao , Jien-Wei Yeh, Peter K. Liaw , Yong Zhang "High-Entropy Alloys- Fundamentals and Applications", 2016, 1st edition, Springer International Publishing Switzerland, Section 1.3.1, 1.3.2 and Chapter 1
5. Yeh J, Chen S, Gan J, Lin S, Chin T, Shun T, et al. Communications: Formation of Simple Crystal Structures in Cu-Co-Ni-Cr-Al-Fe-Ti-V Alloys with Multiprincipal Metallic Elements. Metall Mater Trans A 2004;35A:2533–6.
6. Wang S. Atomic Structure Modeling of Multi-Principal-Element Alloys by the Principle of Maximum Entropy. Entropy 2013;15:5536–48.
7. Yeh J, Chang S, Hong Y, Chen S, Lin S. Anomalous decrease in X-ray diffraction intensities of Cu–Ni–Al–Co–Cr–Fe–Si alloy systems with multi-principal elements 2007;103:41–6.
8. Swalin RA (1972) Thermodynamics of solid, 2nd edn. Wiley, New York, pp 263–266
9. Tong C, Chen Y, Chen S, Yeh J, Shun T, Tsau C, et al. Microstructure Characterization of Al_xCoCrCuFeNi High-Entropy Alloy System with Multiprincipal Elements 2005;36:881–893.
10. Tsai C, Chen Y, Tsai M, Yeh J, Shun T, Chen S. Deformation and annealing behaviors of high-entropy alloy Al_{0.5}CoCrCuFeNi 2010;486:427–35.
11. Swalin RA (1972) Thermodynamics of solids, 2nd edn. Wiley, New York, pp 35–41
12. Shen W, Tsai M, Yeh J. Machining Performance of Sputter-Deposited (Al_{0.34}Cr_{0.22}Nb_{0.11}Si_{0.11}Ti_{0.22})₅₀N₅₀ High-Entropy Nitride Coatings 2015:312–25.
13. Xu J, Wang S, Shang C, Huang S, Wang Y. Microstructure and properties of CoCrFeNi(WC) high-entropy alloy coatings prepared using mechanical alloying and hot pressing sintering. Coatings 2019;9:16.
14. Liang S, Tsai D, Chang Z, Sung H, Lin Y. Applied Surface Science Structural and mechanical properties of multi-element (TiVCrZrHf)N coatings by reactive magnetron sputtering. Appl Surf Sci 2011;258:399–403.
15. Fang Q, Chen Y, Li J, Liu Y, Liu Y. Condensed Matter Microstructure and mechanical properties of FeCoCrNiNbX high-entropy alloy coatings. Phys B Phys Condens Matter 2018;550:112–6.
16. Qiu XW, Zhang YP, Liu CG. Effect of Ti content on structure and properties of Al₂CrFeNiCoCuTi_x high-entropy alloy coatings. J Alloys Compd 2014;585:282–6.
17. Tian LH, Xiong W, Liu C, Lu S, Fu M. Microstructure and Wear Behavior of Atmospheric Plasma-Sprayed AlCoCrFeNiTi High-Entropy Alloy Coating. J Mater Eng Perform 2016;25:5513–21.
18. Lin YC, Cho YH. Elucidating the microstructure and wear behavior for multicomponent alloy clad layers by in situ synthesis. Surf Coatings Technol 2008;202:4666–72.
19. Lin YC, Cho YH. Surface & Coatings Technology Elucidating the microstructural and tribological characteristics of NiCrAlCoCu and NiCrAlCoMo multicomponent alloy clad layers synthesized in situ. Surf Coat Technol 2009;203:1694–701.

WEAR AND FRICTION BEHAVIOR OF NiCrBSi COATINGS AT ELEVATED TEMPERATURE

Nikita Mohite¹, Crystal Liu², Hans Hallen², Bruc Zhang², Kari Westerling²,
Mangesh Patil¹, Amitava Sen¹

¹Höganäs India Pvt. Ltd, Pune, India.

²Höganäs China (Co. Ltd)

Abstract: The increasingly extreme conditions in which components are required to work have led to the use of thermally sprayed and fuse coatings in a lot of industrial applications. Special attention has been paid in NiCrBSi self-fluxing alloy since they provide a high wear and corrosion resistance at high temperatures. Linear reciprocating tribometer (ASTM G-133) is widely used test wherever sliding wear operations in a back and forth motion is involved. In this work, the sliding wear behavior of flame sprayed NiCrBSi alloy specimen during interaction with silicon nitride ball (Si_3N_2) was investigated at elevated temperatures. The parameters like load, temperature, stroke length, frequency and testing time greatly influence the friction and wear properties of the material. The properties were determined at 25N load and 400°C in a controlled atmosphere. The hardness of the material is 60HRC and density of coating of 7.7g/cc was measured by Archimedes principle. The wear volume is determined by optical profilometer and coefficient of friction was observed. In depth- characterization of the wear test specimens was done by SEM (scanning electron microscope). The volume loss observed by optical profilometer was 0.034mm³ and coefficient of friction to be 0.405. SEM analysis shows micro cracks at very few points. Also from the COF Vs time graph, the friction goes on decreasing with time which indicates good sliding wear properties of NiCrBSi alloy at elevated temperatures.

1. Introduction

With the advent of technology, demand for tribosystem capable of running under severe conditions such as at higher relative motions, higher applied loads, at higher temperatures, etc. is increasing. Wear at elevated temperature is a serious problem in a large number of industrial applications such as power generation, transport, materials processing, high temperature bearing, impeller bearing of slurry pumps operated in waste tank, etc. [2-5]. In an effort to improve the performance of materials, attempt is made to use alternate materials or coatings with superior oxidation resistance and enhanced elevated temperature mechanical properties. NiCrBSi alloys for thermal surfacing have played an important role in wear and corrosion protection at elevated temperatures. Essential elements in these alloy are silicon (Si) and boron (B). These elements have several functions, they decrease the melting point of nickel by several hundred

degrees from 1455°C to below 1000°C. They form a light low melting point boron silicate which flows to the surface and protect the melt pool from oxidation. Further they promote wetting of the substrate by reducing oxides of nickel, cobalt, iron and chromium and control surface tension and fluidity of the melt. The low melting point of the NiCrBSi alloys as well as the fluxing effect of the silicon and boron allow these materials to be deposited by flame spray and fuse and powder welding. Apart from nickel, silicon and boron these alloys normally contain chrome (Cr), iron (Fe) carbon (C), and at times molybdenum (Mo), tungsten (W) and copper (Cu). Boron is the primary hard phase forming element while carbon is the second. The microstructure of NiCrSiB alloys consists of relatively ductile Ni-rich matrix with various amounts of hard borides and carbides [7].

The increasingly extreme conditions in which components are required to work have led to

WEAR AND FRICTION BEHAVIOR OF NiCrBSi COATINGS AT ELEVATED TEMPERATURE

the use of thermally sprayed and fuse coatings in a lot of industrial applications. Wear and friction properties plays a vital role in the field of tribology determining components metallurgical and mechanical properties. Linear reciprocating tribometer (ASTM G-133) is widely used test wherever back and forth motion is involved. The present work aims to generate wear data of sprayed and fused NiCrBSi coating and discuss the findings in relation to the coating material structure.

2. Experimental

NiCrBSi alloy has been used as a starting material for thermal spraying and fusing as a surface coating process. Coating is done on 4140 steel substrate. The hardness of the material was 60HRc. The test method describes laboratory procedures for determining the sliding wear of wear-resistant materials using a linear, reciprocating ball-on-flat plane geometry as shown in below fig.1. The direction of the relative motion between sliding surfaces reverses in a periodic fashion such that the sliding occurs back and forth and in a straight line. The principal quantities of interest are the wear volumes of the contacting ball and flat specimen materials; however, the coefficient of kinetic friction may also be measured using the method described.

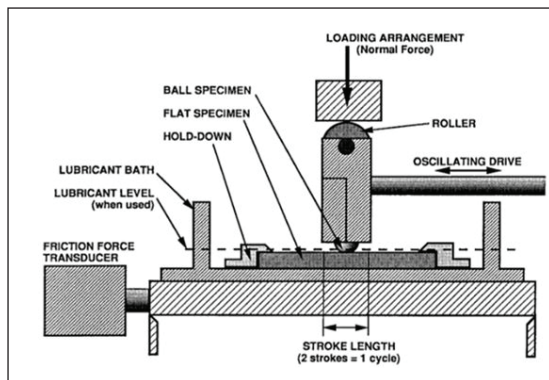


Fig. 1. Schematic Diagram of linear reciprocating sliding wear tribometer

The linear reciprocating sliding wear testing was performed according to ASTM G133 standard [6] using a commercially available tribometer (fig.1). The test specimen blocks were cut in required specification size of 20x20x5mm (Procedure A) blocks to fit the specimen holder in the linear reciprocating tribometer. The test samples achieved an evenly ground surface with surface roughness Ra of close to 0.02 to 0.05µm. The test specimen (lower flat specimen) was sliding against Si₃N₄ ceramic ball (upper specimen) of diameter 10mm. Before tribological tests, both Si₃N₄ balls and coating specimens were cleaned in acetone for 10min. Then, a series of tests were conducted at elevated temperature of 400°C in air, at an oscillating frequency of 5 Hz, a load of 25N, a stroke length of 10mm, a duration of 17mins and a relative humidity of 20-30%. The friction coefficient curves were recorded automatically with a computer attached to the SRV tester. The thickness of the coatings was between 0.6 to over 1mm. The chemical composition of the material used is shown in below table 1.

Table 1 Chemical composition of the material used (Weight %)

C	Si	B	Fe	Cr	Ni	Mo	Cu	W
0.79	4.4	3.2	3.7	14.9	Bal.	-	-	-

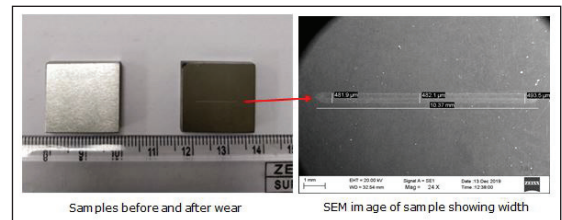


Fig. 2. Overview of sample and SEM image of wear scar

The wear scar investigation was carried out by scanning electron microscope as shown in above fig.2. The volume loss was measured by 3D optical profilometer.

3. Metallography

Microstructure of NiCrBSi alloy as observed in LOM is shown in below fig.3. NiCrBSi alloy

WEAR AND FRICTION BEHAVIOR OF NiCrBSi COATINGS AT ELEVATED TEMPERATURE

consists of γ -Ni (1), Ni₃Si (2), Ni₃B (3) and finely dispersed chromium borides and carbides. Due to the small size and the white colour of the Cr-carbides the microstructure can be better observed in SEM with back scatter electrons as shown in below fig.6.

The grey and black areas in the Secondary electron image corresponds to the chromium carbides and borides in the coating in fig.6

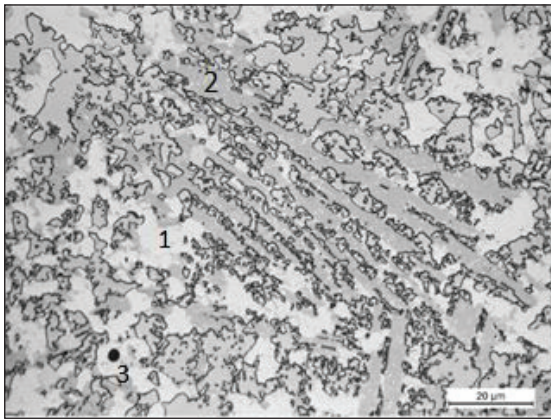


Fig. 3 Light optical Microscopic image of the coated test specimen

4. Results and discussions

Sliding wear test results

The below image fig.4 shows the wear scar in which the wear volume is measured by optical profilometer. By weight loss method, weight gain is observed due to oxidation of substrate. So in such cases, directly volume loss can be achieved by optical profilometer. The results obtained are shown in below table 2. The bulk density of the coating measured by Archimedes principle was 7.7g/cc.

Wear profile by optical profilometer

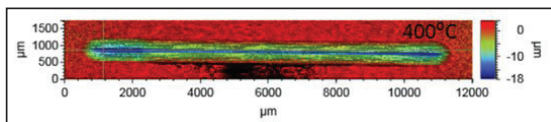


Fig. 4. Image of wear scar of NiCrBSi alloy by optical profilometer at 400°C

Material	Density (g/cc)	Volume loss mm ³ (By Optical profilometer)	Avg. coefficient of friction (COF)
NiCrBSi alloy	7.7	0.034	0.405

Coefficient of friction of NiCrBSi alloy wear sample at 400°C

The below COF graphs in fig. 5 shows that with time friction goes on decreasing which indicates good sliding wear properties of NiCrBSi alloy at elevated temperature of 400°C because of formation of less asperities after certain period of time which means surface turned out smooth which can be observed in below SEM images in fig.6.

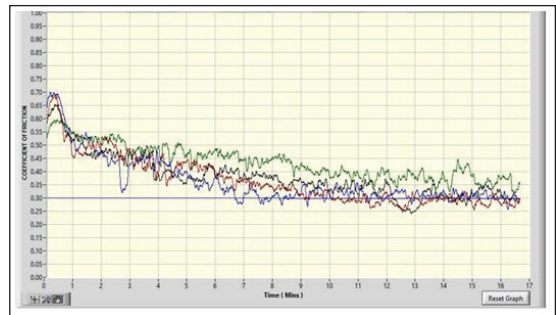


Fig. 5. COF Vs time graph of NiCrBSi alloy at 400°C

Analysis of wear mechanism

In below scanning electron microscopic images, small amount of surface debris and some oxidation can be observed on surfaces (fig.6a and fig.6b). Also micro cracks are seen which may be because of localized plastic deformation and smooth surface observed which indicates reduction in COF over a period of time. (Fig.6c and fig.6d).

WEAR AND FRICTION BEHAVIOR OF NiCrBSi COATINGS AT ELEVATED TEMPERATURE

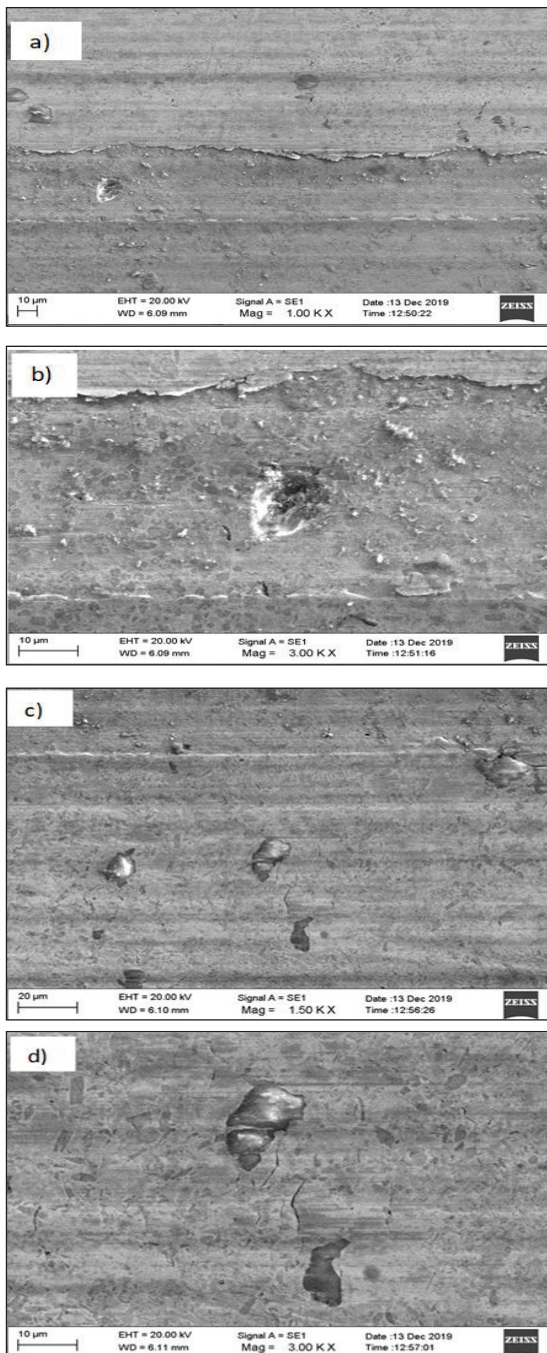


Fig. 6. SEM images of wear scar of NiCrBSi alloy at 400°C

Ploughing and micro cracks observed in some part of wear scar in figure 6d. The micro polishing wear mechanism observed in NiCrBSi alloy could be due to its finer microstructure with smallest carbides and borides. Micro ploughing increases in the materials with higher amounts of austenite.

The wear resistance of the coatings investigated is correlated to the amount of hard phases present in the microstructure.

5. Conclusions

Commercial NiCrBSi material, thermally sprayed and fused alloy coating have been tested for sliding wear according to ASTM G-133 test.

The conclusions drawn are:

- The volume loss obtained by optical profilometer is 0.034mm³ and coefficient of friction to be 0.405 at 400°C.
- Scanning electron microscopic analysis shows that some oxidation has occurred and also NiCrBSi alloy has good sliding wear properties at elevated temperature.
- The grade achieved the higher hardness, 60HRC.
- Coefficient of friction reduces with time because of removal of surface asperities.

6. References

1. A. Pauschitz, Manish Royb , F. Franeka, "Mechanisms of sliding wear of metals and alloys at elevated temperatures", *Tribology International* 41 2008; 584:602
2. Mateos J, Cuetos JM, Vijande R, Fernandej E. *Tribol Int* 2001; 34: 345.
3. Roy M, Pauschitz A, Franek F. *Wear* 2004; 257:799.
4. Taktak S. *Surf Coat Technol* 2006; 201:2230.
5. Jiang X, Liu W, Dong SY, Xu BS. *Surf Coat Technol* 2005; 194:10.
6. ASTM G133-95 (2002), *Standard Test Method for Linearly Reciprocating Ball-on-Flat Sliding Wear*.
7. S: Dizdar, L-Å Nilsson, B. Maroli, Höganäs AB, *Global Developmnet, Höganäs, Sweden*.

DESIGN AND DEVELOPMENT OF ENVIRONMENT FRIENDLY MATERIAL

Natasha Nayak, Harshavardhan Patil and N. B. Dhokey

Department of Metallurgy and Materials Science, College of Engineering, Pune, India.

Abstract: Thermoelectric properties of inexpensive and eco-friendly β - Zn_4Sb_3 were studied and its ability to pose as a peltier device semiconducting material were investigated for a particular temperature range. Single phase polycrystalline sample of β - Zn_4Sb_3 were synthesized by melting in sealed quartz ampoules and water quenching followed by hot pressing of the pre-synthesized powder after grinding. β - Zn_4Sb_3 samples were characterized by XRD analysis. Some physical properties of β - Zn_4Sb_3 were also determined. The β - Zn_4Sb_3 synthesized by this process are found to have high electrical conductivity and a very low thermal conductivity thus making it suitable of peltier application. The Seebeck coefficient and Peltier coefficient of β - Zn_4Sb_3 are measured and calculations show how efficient it can prove to be when used in a peltier module. On the basis of these results an explanation for the maximum theoretical temperature gradient that might be obtained by β - Zn_4Sb_3 at room temperature is suggested.

Introduction

The alarming energy crisis and environmental issues in the recent years have resulted in the renewed interest in thermoelectric materials for possible application in direct conversion between heat and electricity. Thermoelectric devices are reliable, operate unattended in hostile environments and are also environmentally friendly; but new more efficient materials are needed to expand their range of applications. Increasing the figure of merit ZT of the materials used in thermoelectric devices is greatly influencing the growth in the commercial applications of these peltier based devices.^[1] Depending on the temperature range of application, the established thermoelectric materials can be divided into three categories. Bismuth telluride and its alloys work around the room temperature and have a maximum operating temperature of about 500K. In the intermediate temperature range of 600K to 900K, PbTe-based alloys and TAGS (Te-Ag-Ge-Sb) are the most efficient materials. At higher temperatures of about 1000K to 1300K, Si-Ge alloys are used in power generation devices mainly for space applications.^[2]

Based on theoretical considerations and

literature data, a number of new potentially high performance thermoelectric materials have to be identified. As a part of the broad search for more eco-friendly thermoelectric materials, we have developed a process for the synthesis of a semiconducting compound, Zn_4Sb_3 .^[3] In the Zn-Sb system, the three compounds that can be identified are: first, ZnSb decomposing peritectically at 819K, second, Zn_4Sb_3 melting congruently at 836K, and third, Zn_3Sb_2 melting congruently at 839K.^[4] For Zn_4Sb_3 , three modifications are known: α - Zn_4Sb_3 , β - Zn_4Sb_3 , χ - Zn_4Sb_3 which are respectively stable below 263K, between 263K and 765K, and above 765K. β - Zn_4Sb_3 has a hexagonal rhombohedral crystal structure, space group R3C, with $a=1.2231$ nm and $c=1.242$ nm^[13, 15]. Because of its relatively complex structure low thermal conductivity values are expected.

We have synthesized single phase, polycrystalline samples of β - Zn_4Sb_3 by the powder metallurgy route to obtain the best results. The physical, mechanical and thermoelectric properties of these samples are yet to be examined. Investigations are to be conducted in order to assess its temperature stability and its usefulness for thermoelectric applications

Experimental

Single phase, polycrystalline samples of β - Zn_4Sb_3 were prepared by the powder metallurgy route. First, zinc pellets (99.99% pure) and antimony shots (99.99% pure) were converted into powder by cryogenic process using liquid nitrogen. Both the powders were taken in stoichiometric ratio and sealed in quartz ampoules with argon gas. The sealed quartz ampoules were placed in a furnace at a temperature of 1023K. The melts were held at 1023K for about 2 hours for homogenization. After the homogenization interval, the sealed quartz ampoules containing the melt were quenched in water at room temperature. The quartz ampoules were broken to obtain the material synthesized. The resulting ingots were ground in an attrition mill and analyzed by X-Ray Diffractometry (XRD), Bruker (D8 VENTURE). The XRD results were verified and it was found that the powders so obtained after quenching were of β - Zn_4Sb_3 . The powder was then sieved and only grains with a size of 125 μm or less were retained for further processing. The pre-synthesized powders were then hot-pressed into cylindrical samples of 10mm in diameter and 11mm in length. The hot-pressing was conducted in graphite dies at 673K. The density of the samples was measured by ASTM standard B962-08 using Archimedes' principle. The samples were crack-free and of good mechanical strength. A total of 10 samples were fabricated.

Results and Discussion

Some properties of β - Zn_4Sb_3 at room temperature are listed in Table 1.

Property	Units	β - Zn_4Sb_3
Melting Point	K	836
Density	$g\ cm^{-3}$	6.077
Lattice Parameter	nm	a = 1.2231 c = 1.2428

Density obtained through the ASTM Standard process was found to be $5.82\ g\ cm^{-3}$. This accounts to 95 to 97% of the theoretical density.

The SEM-EDS analysis depicts the uniform distribution of Zn and Sb throughout the powder obtained after attrition milling for 6 hours (Fig 1 to Fig 3). The size of the powder particles is confirmed to be equal to or less than $125\ \mu m$ though SEM (Fig 4 and Fig 5).

The plot obtained by XRD confirms the presence of β - Zn_4Sb_3 phase throughout (Fig 6). Some amount of silicon encountered can be rectified by taking care during the retrieval of quenched ingot from silica glass ampoules.

Spectrum	EDS
Zn (wt%)	55.06
Sb (wt%)	39.91
Si (wt%)	0.16
Phase	β - Zn_4Sb_3



Fig 1: SEM image of the powder (<125 μm) retained after 6 hours of attrition milling at a magnification of 500x

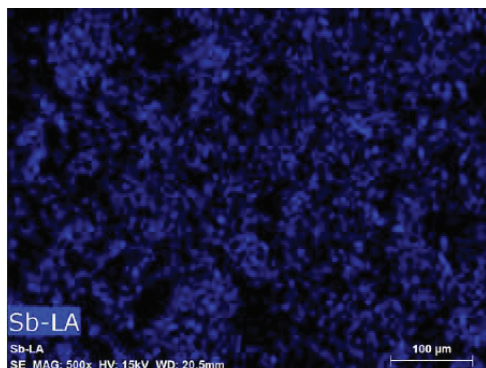


Fig 2: Elemental Mapping of Sb showing its contribution in the composition of the powder produced.

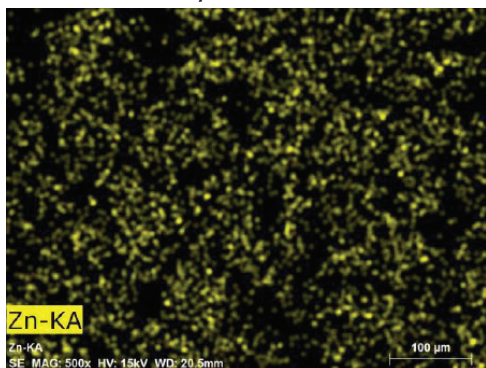


Fig 3: Elemental Mapping of Zn showing its contribution in the composition of the powder produced.

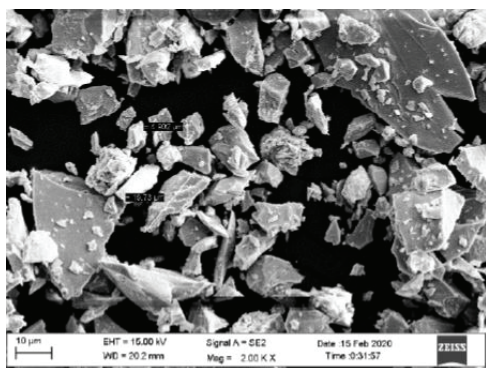


Fig 4: SEM image of the powder (<125μm) retained after 6 hours of attrition milling at a magnification of 2000x depicting the size of particles.

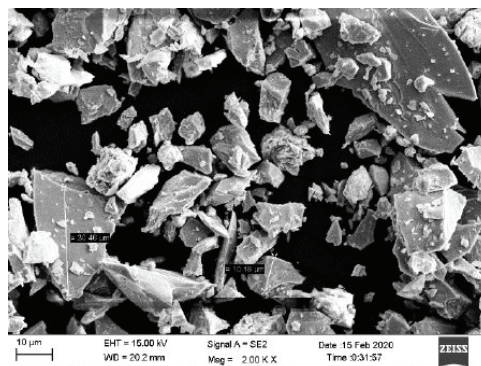


Fig 5: SEM image of the powder (<125μm) retained after 6 hours of attrition milling at a magnification of 2000x depicting the size of particles.

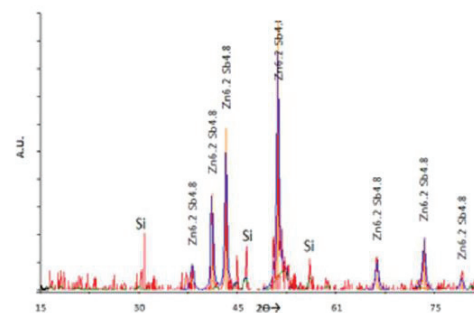


Fig 6: XRD Analysis results showing the peaks of β - Zn_4Sb_3 . A few peaks of silicon are also obtained.

As evident from XRD and presence of Si peaks it is revealed that synthesis condition is not fully optimized.

Conclusions

The β - Zn_4Sb_3 synthesized by this process are found to have high electrical conductivity and a very low thermal conductivity thus making it suitable of peltier application. The Seebeck coefficient and Peltier coefficient of β - Zn_4Sb_3 are measured and calculations show how efficient it can prove to be when used in a peltier module. On the basis of these results an explanation for the maximum theoretical temperature gradient that might be obtained by β - Zn_4Sb_3 at room temperature is suggested.

References

1. Yunosuke MAKITA, ¹Zhengxin LIU, ¹Teruhisa OOTSUKA, ¹Naotaka OTOGAWA, ¹Masato OSAMURA, ¹Yasuhiro FUKUZAWA, ²Ryo KURODA, ¹Yasuhiko NAKAYAMA, ²Yasuyuki HOSHINO, ³Hisao TANOUE, "Beta Iron Disilicide (β -FeSi₂) As an Environmentally Friendly Semiconductor for Space Use"
2. Vähänissi, Ville & Haarahiltunen, Antti & Ylikoski, Marko & Savin, Hele. 2014. Gettering of Iron in Silicon Solar Cells with Implanted Emitters. *IEEE Journal of Photovoltaics*. Volume 4, Issue 1. 142-147. ISSN 2156-3381 (printed).DOI:10.1109/jphotov.2013.2285961.4
3. Bag A., Mukherjee C., Mallik* S. and Maiti C. K., "Low Frequency Noise in Iron Disilicide Heterojunction Solar Cells" *J. Appl. Phys.* 1963, 34, pp 1648-1649.
4. Mozharivsky Y., Perchersky A.O., Bud'ko S., Miller G.J., *Chem. Mater.* 16 (2004) 1580-1589
5. Kasap S. O., *Principles of Electronic Materials and Devices*, pp 400- 490

COMMERCIAL USE OF SMC IN ELECTRICAL BUSES

R. Guo¹, M. Nie¹, S. Grenier², D. Tremblay³

¹Rio Tinto Iron & Titanium, Suzhou, China

²Rio Tinto Metal Powders, Sorel-Tracy, Canada

³DANA TM4, Boucherville, Canada

Introduction

SMCs have been around for many decades. However, it is only recently that major car manufacturers are taking actions and massively investing efforts and resources into their new vision of the electrical vehicle (EV) motor. The change in focus from the traditional internal combustion engine (ICE) to the EV motor came about from legislations which have been adopted in many countries and which will ban the sale of new vehicles equipped with ICE engines in the near future. These legislative changes have themselves been brought about by consumers concerns over the environment and their dependence to fossil fuels.

This presentation describes an example of a commercial application developed by DANA-TM4, the CNRC (Canada National Research Council) and, Rio Tinto Metal Powders. In that application (electrical buses), SMC were incorporated in the motor design to improve its performance.

General Approach

There currently exists a multitude of known EV motor designs; each of them being characterized by a series of advantages and disadvantages. In many of these designs, Soft Magnetic Composites (SMC) represent one of the components considered, the two others being Permanent Magnets (PM) and Laminated Components (LC).

The general approach used by car manufacturers is to start with a standard EV motor platform (e.g. axial flux, radial flux or transverse flux) and build upon it using a team of experts. Some of these experts, such as magnetic flux modeling specialists, are part of a profession that did not exist a few decades ago. Nowadays, these modeling experts enter the mechanical and magnetic properties of the SMC, PM and LC

materials in their modeling software and use these as the building blocks of their designs. Computers play an instrumental role in the incremental EV design improvement process. Indeed, the 3D nature of the magnetic flux lines is best taken advantage of using a computer; an essential tool to overcome the limitations resulting from the 2D views that plans offer and that our brains are used at tackling.

It is with a similar approach that a team composed of scientists from DANA-TM4 have come-up with the conception of an EV motor with an external rotor, the SUMO™ family of motor, a design which maximizes torque. Besides optimizing the performance of the engine using parameters such as W/kg, kg/kW, or kW/m³, designers must also look at a parameter that is crucial to the end user, that is \$/kW. It is with this in mind that the option of using SMC to replace part of the costly PM materials was considered.

Commercial Application

In excess of 12000 motors from the SUMO™ family have been produced. The entire fleet of electric buses (Figure 1) equipped with these motors have driven over 950 million kilometers since they initially hit the roads in service in China.



Fig. 1 : Photograph of an electric bus(1) equipped with a motor from the SUMO™ family.

The extended distance travelled over the years by these EV motors is a testimony of their reliability, as well as of the reliability of SMC components in commercial applications.

Design

The EV motor, located in the rear of the buses, uses a proprietary external rotor design(2) to maximize torque and provide a compact source of power.

The design of this motor went through several phases over the years. One of the initial motor design was an external rotor with its interior covered with PM. As indicated earlier, as part of the final design, OEMs must also look at the \$/kW parameter. With the recent increase in price for PM, studies were conducted to see if some of the costly PM components could be replaced with much less expensive SMC (Figure 2).

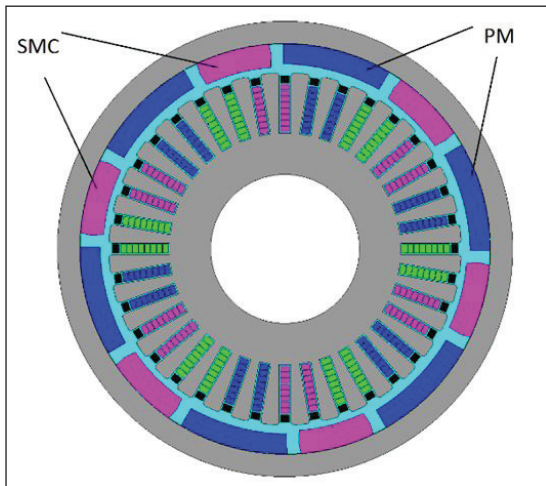


Fig. 2 : Schematic representation of the combination of use of PM and SMC in a PMVR (Permanent Magnet Variable Reluctance) SUMO™ motor(2).

Properties of the SMC (EM-5)⁽³⁾ material used in this motor is presented in Table 1. The mechanical and magnetic properties of the SMC material were not maximized (eg. TRS, μ_{max} and B_s) or minimized (e.g. Fe losses and H_c) for the sake of producing a « superior » material.

Instead, the properties of the EM-5 materials were tailored to match the requirements of the optimized modeling trials determined by the motor designers.

Table 1 : Main Properties of the EM-5 SMC.

	H_c	μ_{max}	B_s (@ 150 Oe)	Fe losses @ 1T		TRS
				60 Hz	1000 Hz	
EM-5	297 A/m	401	1,47 T	6,5 W/kg	160 W/kg	47 MPa

The incorporation of SMC in this motor design has not only resulted in an overall lower production cost, but has also yielded an additional benefit; improved motor performance. This presentation will go over this application and discuss the benefits observed; a good example of the advantages that can sometime be obtained by combining the various characteristics of PM, SMC and LC.

References

- 1) www.danatm4.com
- 2) WIPO - R. Shi, A. Gharakhani, M. Houle, International patent WO 2016/14552 A1, DANA-TM4.
- 3) EM-5 is produced at Rio Tinto Iron & Titanium, Suzhou, China.

PREPARATION AND ELECTROCHEMICAL CHARACTERIZATION OF Ca DOPED $\text{Nd}_2\text{NiO}_{4+\delta}$ SOLID OXIDE FUEL CELL CATHODE MATERIAL

Pranjal Gandhrea, R K Lenka^b, P K Patro^b, L Muhmood^a, and T Mahata^b

^aK.J.Somaiya College of Engineering, Vidyavihar, Mumbai.

^bPowder Metallurgy Division, Bhabha Atomic Research Centre, Vashi Complex, Mumbai.

Abstract: Solid oxide fuel cells (SOFC) are all oxide electrochemical systems which converts chemical energy directly to electrical energy in an efficient manner. Among the emerging technologies to address greenhouse gas emission, hydrogen fuel cell is a prospective candidate in the race. In the present study, four compositions of $\text{Nd}_2\text{-xCa}_x\text{NiO}_{4+\delta}$ ($x=0.2, 0.4, 0.5, 0.6$) were synthesized via solid state route by mixing constituent precursor oxides/carbonates followed by calcining at 1150°C for 10 h. Phase purity of the powder has been confirmed by analyzing the X-ray diffraction pattern. Electrical conductivity measured by DC 4-probe method shows conductivity in the range 40-125 S/cm for the calcium doped samples in the intermediate temperature region of fuel cell. Maximum electrical conductivity is observed for $x=0.4$ composition. Symmetric cells are prepared using the above cathode compositions and gadolinium doped ceria (GDC) as electrolyte. Area Specific Resistance (ASR) of these symmetric cells was calculated from the measured impedance data from 600°C to 850°C. A minimum in the ASR value (0.3 ohm.cm²) was obtained for $x=0.2$ composition at 850°C. From the initial results, it can be concluded that small Ca doping is favourable for enhancing the electrochemical properties of $\text{Nd}_2\text{NiO}_{4+\delta}$ cathode materials for SOFC applications.

Introduction

Solid oxide fuel cells (SOFC's) are clean source of energy produced from direct conversion of chemical energy into electrical energy in an efficient manner^[1,2]. The other notable advantages are modular in construction and excellent fuel flexibility especially for hydrocarbon-based fossil fuels. Though the performance of SOFC's are better at higher temperatures; material compatibility remains a challenge. In the intermediate temperatures (i.e. 650°C to 850 °C) the performance of cathode limits the overall fuel cell performance. Considerable investigations have been done on various perovskite-type oxides to improve the cathode performance at intermediate temperatures [3,4,5]. Apart from oxides, some A_2BO_4 oxides with the perovskite-related K_2NiF_4 type structure are explored as plausible cathode material owing to their high oxygen ion diffusivity^[6,7]. In this family of materials, most of the work is focused on mixed conducting materials related

to rare earth nickelates. $\text{Nd}_2\text{NiO}_{4+\delta}$ (NNO) as a cathode exhibits promising electro catalytic activity towards oxygen reduction reactions, owing to incorporation of excess oxygen in the lattice^[8]. NNO is also considered to be a mixed ion electron conductor (MIEC) with appreciable ionic conductivity attributed to the presence of highly mobile interstitial oxygen in its structure^[9]. $\text{Nd}_2\text{NiO}_{4+\delta}$ material showed to have a δ value up to 0.25 depending on the method of synthesis^[10]. Thermal expansion coefficient of $\text{Nd}_2\text{NiO}_{4+\delta}$ is close to the frequently SOFC electrolyte materials (GDC and YSZ). In the A_2BO_4 compounds, substitution at B site simultaneously affect the oxygen over-stoichiometry and the transport properties. Electrical conductivity and catalytic properties of $\text{Nd}_2\text{NiO}_{4+\delta}$ can be further improved by doping with aliovalent cation like Sr^[11]. Khandale et al have measured a decrease in ASR value in $\text{Nd}_2\text{-xSr}_x\text{NiO}_{4+\delta}$ ($x=0.2$) composition with respect to the undoped nickalate. It has been observed that with further increase in the dopant concentration,

PREPARATION AND ELECTROCHEMICAL CHARACTERIZATION OF Ca DOPED $\text{Nd}_{2-x}\text{Ca}_x\text{NiO}_{4+\delta}$ SOLID OXIDE FUEL CELL CATHODE MATERIAL

there is a decrease in the electrical conductivity and catalytic property also [12]. Electrical conductivity and structural characterization of Ba, Sr and Ca doped $\text{Nd}_{2-x}\text{NiO}_{4+\delta}$ material system is studied in literature [13]. However, electrochemical properties are not extensively studied for SOFC applications. Dopant of higher size compared to Nd is generally preferred to reduce the lattice strain in $\text{Nd}_{2-x}\text{NiO}_{4+\delta}$. However, in the present investigation a Ca (similar in size as Nd) is chosen in different ratios and its effect on cathodic properties is studied.

Experimental Section

Powder synthesis and characterization

Cathode compositions $\text{Nd}_{2-x}\text{Ca}_x\text{NiO}_4$ ($x=0.2, 0.4, 0.5$ and 0.6) were synthesized via solid-state route by mixing required amounts of neodymium oxide (Nd_2O_3) (IRE Limited, purity 99.9 %), nickel oxide (NiO) (SD Fine chemicals, Purity 99.9%) and calcium carbonate (CaCO_3) using a planetary ball mill. The milling process was performed for 2hrs in ethanol medium in a zirconia pot using zirconia balls. The powder mixtures were calcined at 1150°C for 10h to obtain the desired single phase. Henceforth the cathode compositions $\text{Nd}_{1.8}\text{Ca}_{0.2}\text{NiO}_4$, $\text{Nd}_{1.6}\text{Ca}_{0.4}\text{NiO}_4$, $\text{Nd}_{1.5}\text{Ca}_{0.5}\text{NiO}_4$ and $\text{Nd}_{1.4}\text{Ca}_{0.6}\text{NiO}_4$ were abbreviated as NCN2, NCN4, NCN5 and NCN6 respectively. Phase purity of the powders was confirmed from the X-ray diffraction pattern of the powder samples. Diffraction patterns were collected using an X-ray Diffractometer (INEL, France) using Cu K-alpha radiation from 20-90 degree. Particle size of the powder was measured using a laser diffraction particle size analyzer (CILAS, France).

Compatibility, Electrical and electrochemical characterization:

Compatibility of the series of new cathode material with GDC electrolyte was checked by

mixing (1:1 wt %) of NCN5 cathode powder with electrolyte powder followed by calcinations at 1250°C . The composite powder was characterized by x-ray diffraction for possible interactions. Peak positions are compared with the peaks from the cathode compositions and GDC electrolyte.

For all cathode compositions, bar shaped pellets were made for electrical conductivity measurement using a rectangular die assembly and a uniaxial die press. The samples were sintered at 1250°C for 3 hrs. Contact points are developed by silver paste at the two end faces of the rectangular bar and on two points in between the pellet which are at a minimum of 1cm apart. Four Probe-DC conductivity of the bar shaped samples were carried out using a ProboStat(NORCES) test unit and a Keithley DC source-measure unit. Green circular pellets of all powder compositions of 8mm dia and 6mm length were prepared using a uniaxial die arrangement. Linear shrinkage pattern was recorded from room temperature to 1250°C in flowing air atmosphere using a thermo mechanical analyzer.

Symmetric cells were prepared over a 10 mm GDC pellets. Circular pellets of GDC were prepared using a uniaxial die press followed by sintered at 1250°C for 3 hrs. The $\text{Nd}_{2-x}\text{Ca}_x\text{NiO}_4$ powders were mixed with terpineol to form slurry, and subsequently screen printed on both sides of the sintered GDC pellet. The pellet was then sintered at 1200°C for 3hrs. Silver paste was applied on the both surfaces of the electrode for better current collection. Complex impedance of the symmetric cells was measured using ZIVE MP5 multi-channel electrochemical workstation from 600°C to 850°C . Area specific resistance (ASR) was calculated from the complex impedance data.

PREPARATION AND ELECTROCHEMICAL CHARACTERIZATION OF Ca DOPED $\text{Nd}_2\text{NiO}_{4+\delta}$ SOLID OXIDE FUEL CELL CATHODE MATERIAL

Results and Discussion

Synthesis and Compatibility study

The constituent precursor powder mixture after ball milling was dried followed by calcinations at 1150°C for 10 hours to get the required phase. Fig.1 shows the x-ray diffraction pattern of the calcined powders. The diffraction patterns can be indexed with respect to the JCPDF file number 01-088-0761. Apart from the desired phase, no detectable extra phase was observed in the x-ray diffraction pattern indicating phase purity of the material. Similar peak pattern has also been observed by Pikalov et al [14] for Ca doped $\text{Nd}_2\text{NiO}_{4+\delta}$ ceramics. Fig.2 shows the x-ray diffraction pattern of NCN5 and GDC mixture calcined at 1250°C . Apart from cathode and electrolyte peaks, no extra peaks is observed in the diffraction pattern. This demonstrates a good chemical compatibility between Ca doped $\text{Nd}_2\text{NiO}_{4+\delta}$ cathodes with GDC electrolyte material. Average sizes of the cathode powders measured by laser diffraction experiment are close to one micron. Particle size (d_{50}) of GDC electrolyte powder is around 1.2 micron. Particle size of the cathode materials are in the same range as that of the electrolyte powder.

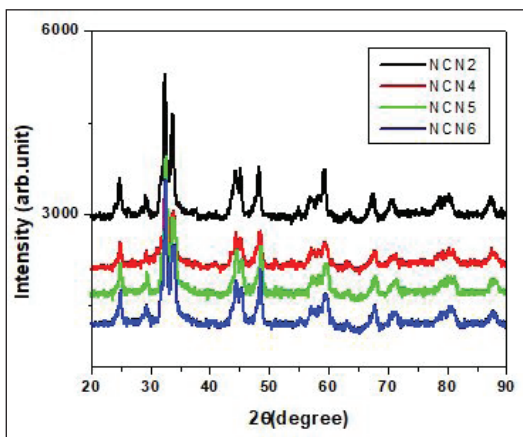


Fig.1: X-ray diffraction pattern of $\text{Nd}_{2-x}\text{Ca}_x\text{NiO}_4$ ($x=0.2, 0.4, 0.5$ and 0.6)

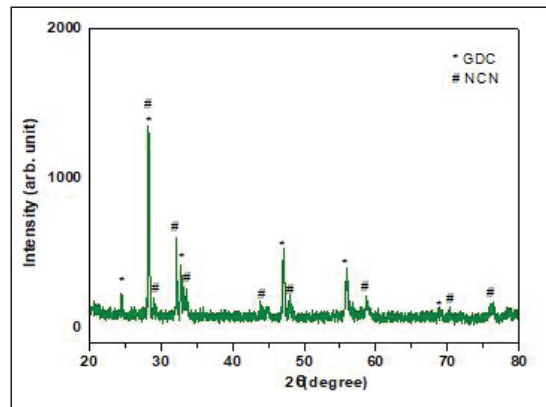


Fig.2: X-ray diffraction pattern showing compatibility between NCN5 and GDC electrolyte

Functional Property measurement

Electrical Conductivity: Electrical resistivity of the samples were recorded both during heating and cooling of the samples from room temperature to 800°C . However, more stable data during cooling is presented in this work. The change in electrical conductivity of the sample with temperature is shown in Fig.3.

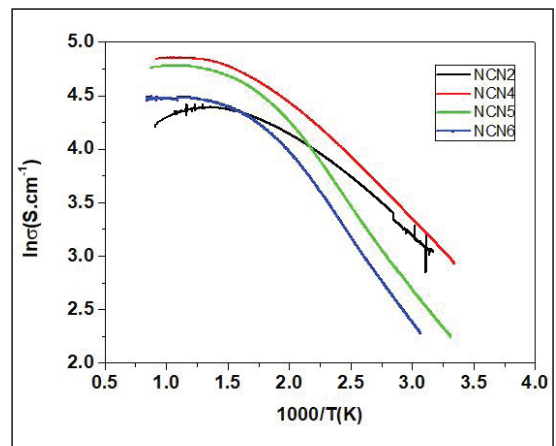


Fig.3: Conductivity variation of Ca doped samples with temperature

It has been observed that electrical conductivity increases with temperature and attains saturation

PREPARATION AND ELECTROCHEMICAL CHARACTERIZATION OF Ca DOPED Nd₂NiO_{4+δ} SOLID OXIDE FUEL CELL CATHODE MATERIAL

at high temperature. This change in trend can be correlated to semiconducting to metallic phase transition as explained by Khandal et.al in Sr doped Nd₂NiO_{4+δ} samples [12]. Among all the compositions studied, maximum in the electrical conductivity is observed for NCN4. With further increase in the dopant concentration, electrical conductivity decreases. Similar trend in the electrical conductivity data has been obtained for Ca doped Nd₂NiO_{4+δ} by Pikalov et.al^[14].

Conductivity mechanism and its trend can be better understood with the help of defect chemistry model. Total conductivity associated with the transfer of electrons (e') and holes (h') can be expressed as follows:

$$\sigma = e c \mu \quad (1)$$

Where e is the charge of the electron or hole, c is the concentration of the charged species and μ the mobility.

It has been observed that interstitial oxygen content decreases with increase in the dopant concentration. With this loss of interstitial oxygen, both oxygen vacancy and hole is generated in the sample. This can be explained by the KrögerVink notation, as follows:



With doping, the concentration of Ni³⁺(hole) increases, hence conductivity increases. For NCN5 the concentration of hole (Ni³⁺) are equal to Ni²⁺. With further increase in calcium concentration, electronic charge carriers compensate with the holes. Hence, conductivity value decreases for NCN6. Conductivity maximum is observed for NCN4 in our work and a similar trend in the conductivity is reported in literature [14]. As synthesis method has great influence on the oxygen content and functional properties, this small change in the peak of conductivity curve is expected.

Linear shrinkage curve of Ca doped Nd₂NiO_{4+δ} samples with temperature is shown in Fig.4. It has been observed that with Ca incorporation, there is a shift in the shrinkage initiation temperature and shrinkage rate decreases with Ca doping. Low temperature sintering is beneficial for better electrode performance. Higher the sintering temperature more is the probability of interaction between electrode and other cell components. Also low temperature sintering has certain advantages like large choice of materials for cell components and greater catalytic activity. Compositions with lower doping level are helpful to achieve lower sintering temperature of the electrode layer. This shrinkage rate is inversely proportional to the electrical conductivity, i.e. directly proportional to the concentration of interstitial oxygen content. Defects developed due to this interstitial oxygen may be responsible for the greater diffusion of ions in the electrodes.

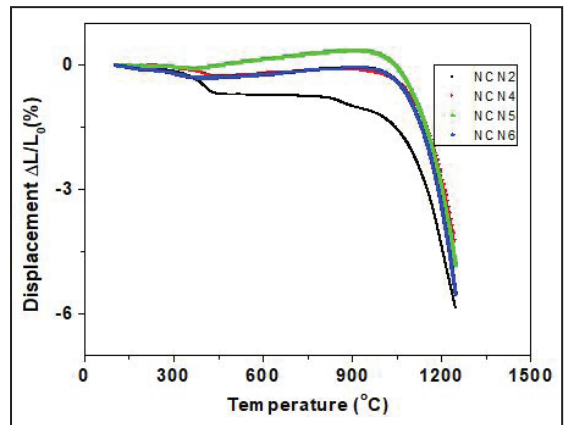


Fig.4: Linear shrinkage curve of Ca doped NNO with temperature

Oxygen reduction reaction from ASR measurement

Impedance plot of the symmetric cells measured in the frequency range 1MHz to 0.1Hz and temperature range 700oC to 850oC in static air

**PREPARATION AND ELECTROCHEMICAL CHARACTERIZATION OF Ca DOPED
Nd₂NiO_{4+δ} SOLID OXIDE FUEL CELL CATHODE MATERIAL**

is shown in Fig.5 (a-c). From the intercept of the impedance curve with the real axis, area specific resistance value was calculated taking account of the cathode area. Area specific resistance decreases with temperature due to increase in catalytic activity of the cathode material. Higher the operating temperature better is the performance. Table-1 represents a summary of the ASR values with temperature for all the cathode compositions. It has been observed that ASR value is lowest for NCN2 and highest for NCN4. This trend is opposite to the electrical conductivity curve. Catalytic properties of the air electrode depend on the ability of oxygen to reduce at the cathode-electrolyte interface. Oxygen vacancies and oxygen interstitial are responsible for this reduction reaction. From equation-2 it can be seen that one mole of oxygen release from the interstitial will release one mole of oxygen vacancies. Hence, concentration of oxygen vacancy increases and concentration of oxygen interstitial decreases with Ca doping. Activation energy for oxygen reduction reaction via interstitial oxygen is lower compared to oxygen vacancies. Hence lowest ASR value is obtained for NCN2.

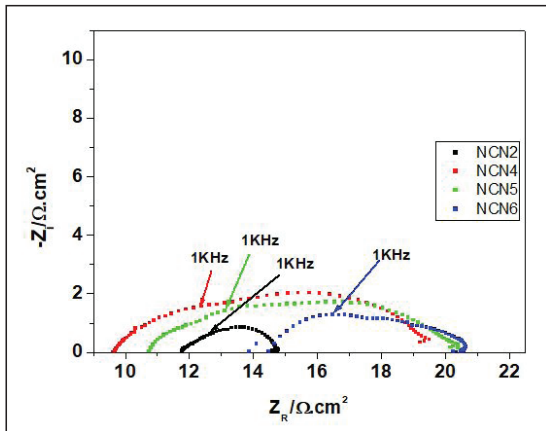


Fig. 5.(a): Area specific resistance of Ca-NNO at 750°C

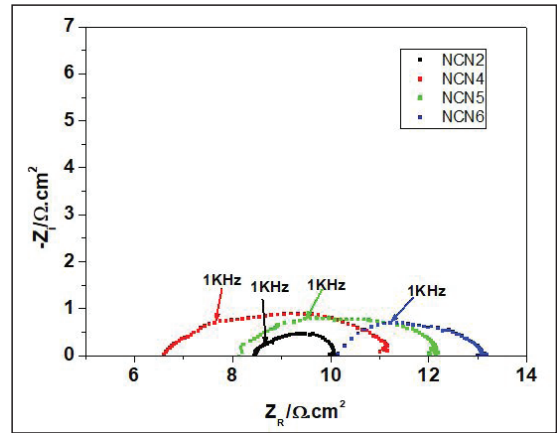


Fig. 5.(b): Area specific resistance of Ca-NNO at 800°C

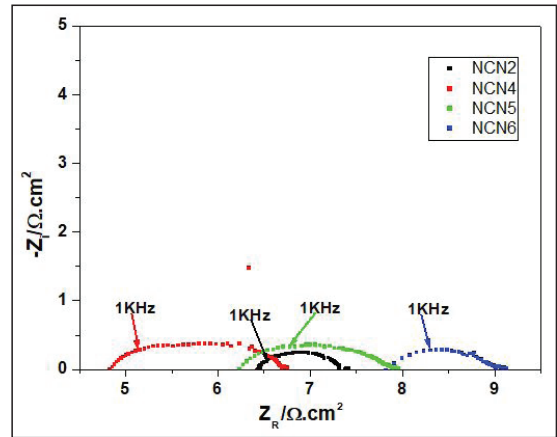


Fig. 5.(c): Area specific resistance of Ca-NNO at 850°C

Table-1: Cell ASR values of cathode compositions at different temperatures

Composition	ASR (Ω·cm ²)					
	600°C	650°C	700°C	750°C	800°C	850°C
NCN2	12.48	5.85	2.34	0.975	0.546	0.312
NCN4	52.65	21.06	12.87	3.9	1.872	0.78
NCN5	92.04	31.98	10.14	3.51	1.56	0.702
NCN6	46.02	18.72	6.24	2.73	1.092	0.546

PREPARATION AND ELECTROCHEMICAL CHARACTERIZATION OF Ca DOPED Nd_{2-x}NiO_{4+δ} SOLID OXIDE FUEL CELL CATHODE MATERIAL

Arrhenius plot of area specific resistance with temperature is shown in Fig.6 and activation energy for oxygen reduction reaction is calculated from the slope. NCN2 has the lowest activation energy (86kJ/mol) for oxygen reduction reaction. Activation energy of Ca doped NNO samples are close to some of the high performance cathode materials like BSCF, LSCF and LNO cathode materials. The scanning electron micrograph of a symmetric cell showing electrode-electrolyte interface is shown in Fig. 7. Porous electrode structure (thickness ~35 μm) adherent to electrolyte is observed from the micrograph. Porosity in the cathode material is essentially helpful for the transfer of reactant and release of product gases at the electrode-electrolyte interface.

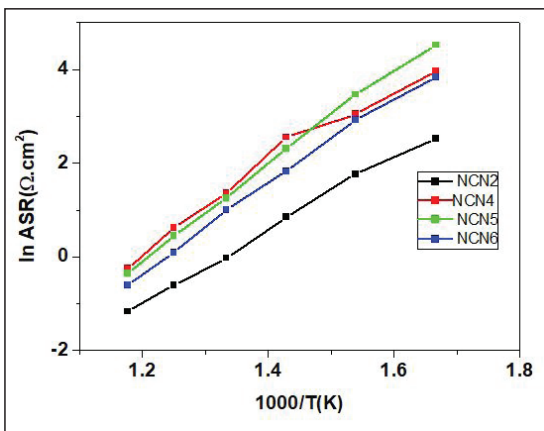


Fig.6: Arrhenius plot of polarization with temperature

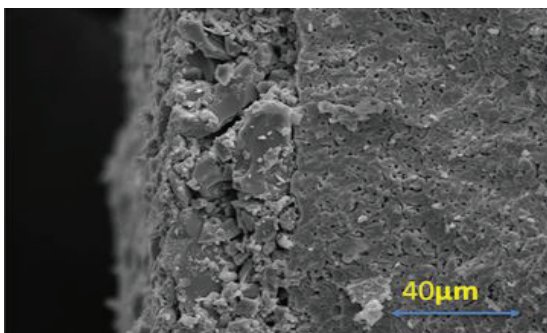


Fig.7: SEM micrograph of a symmetric cell (NCN2)

Conclusion:

Phase pure new cathode compositions Nd_{2-x}Ca_xNiO₄ (x=0.2, 0.4, 0.5, 0.6) could be synthesized via solid state route by calcining the reactant mixture in air atmosphere at 1250°C. Nd_{2-x}Ca_xNiO₄ cathode is compatible to GDC electrolyte at high temperatures. Calcium doping enhances the electrical conductivity of the cathode material by generation of holes. Electrical conductivity more than 40S.cm⁻¹ has been obtained for all compositions, in the operating temperature region of the fuel cell. Area specific resistance measurement shows decline trend in the catalytic activity with calcium doping. Lowest activation energy for oxygen reduction reaction is calculated to be around 86kJ/mol for NCN2 composition. From the initial studies it can be inferred that a small amount of Ca doping enhances both the electrical conductivity and catalytic property.

References:

- [1] Viswanathan B, *Fuel Cell: Principles and applications*, CRC press, 2008.
- [2] W. Vielstich, H. A. Gasteiger, A. Lamm (Editors), *Hand book of fuel cells, Fundamentals, Technology and applications*, John Wally & sons Chichester, England, 2003
- [3] Shoroshi Dey; Jayanta Mukhopadhyay; Raja KishoraLenka; Pankaj Kumar Patro; Abhijit Das Sharma; TarasankarMahata; Rajendra N. Basu, *Synthesis and characterization of Nanocrystalline Ba_{0.6}Sr_{0.4}Co_{0.8}Fe_{0.2}O₃ for application as an efficient anode in solid oxide electrolyser cell*, *International Journal of Hydrogen Energy* 45 (2020)3995
- [4] K. Dumaisnil, D. Fasquelle, M. Mascot, A. Rolle, P. Roussel, S. Minaud, B. Duponchel, R.N. Vannier, J.C. Carru, *Synthesis and characterization of La_{0.6}Sr_{0.4}Co_{0.8}Fe_{0.2}O₃ films for solid oxide fuel cell cathodes*, *Thin Solid Films* 553 (2014) 89–92
- [5] Atanu Dutta, Jayanta Mukhopadhyay, R.N. Basu, *Combustion synthesis and characterization of LSCF-based materials as cathode of intermediate temperature solid oxide fuel cells*, *Journal of the European Ceramic Society* 29 (2009) 2003–2011

PREPARATION AND ELECTROCHEMICAL CHARACTERIZATION OF Ca DOPED $\text{Nd}_2\text{NiO}_{4+\delta}$ SOLID OXIDE FUEL CELL CATHODE MATERIAL

- [6] V. V. Vashook, I. I. Yushkevich, L. V. Kokhanovsky, L. V. Makhnach, S. P. Tolochko, I. F. Kononyuk, H. Ullmann, H. Altenburg, *Composition and conductivity of some nickelates*, *Solid State Ionics* 119 (1999) 23-30
- [7] J. D. Jorgensen, B. Dabrowski, Pei shiyu, *Structure of the interstitial oxygen defect in $\text{La}_2\text{NiO}_{4+\delta}$* *Phys. Rev. B* 40 (1989) 2187-2191.
- [8] F. Mauvy, J.-M. Bassat, E. Boehm, J.P. Manaud, P. Dordor, J.C. Grenier, *Oxygen electrode reaction on $\text{Nd}_2\text{NiO}_{4+\delta}$ cathode materials: impedance spectroscopy study*, *Solid State Ionics* 158 (2003) 17-28
- [9] X. Li, N.A. Benedek, *Enhancement of ionic transport in complex oxides through soft lattice modes and epitaxial strain*, *Chem. Mater.* 27 (2015) 2647-2652
- [10] E. Boehm, J.M. Bassat, P. Dordor, F. Muvy, J.C. Grenier, Ph. Stevens, *Oxygen diffusion and transport properties in non-stoichiometric $\text{Ln}_2\text{NiO}_{4+\delta}$ oxides*, *Solid State Ionics* 176 (2005) 2717-2725.
- [11] Li-Ping Sun, Qiang Li, Hui Zhao, Li-Hua Huo, Jean-Claude Grenier, *Preparation and electrochemical properties of Sr-doped Nd_2NiO_4 cathode materials for intermediate-temperature solid oxide fuel cells*, *Journal of Power Sources* 183 (2008) 43-48
- [12] A. P. Khandale, J. D. Punde, S. S. Bhoga, *Electrochemical performance of strontium-doped neodymium nickelate mixed ionic-electronic conductor for intermediate temperature solid oxide fuel cells*, *J Solid State Electrochem* (2013) 17:617-626
- [13] J.P. Tang, R.I. Dass, A. Manthiram, *Comparison of the crystal chemistry and electrical properties of $\text{La}_{2-x}\text{A}_x\text{NiO}_4$ (A = Ca, Sr, and Ba)*, *Materials Research Bulletin* 35 (2000) 411-424
- [14] S.M. Pikalov, L.B. Vedmid, E.A. Filonova, E. Yu. Pikalova, J.G. Lyagaeva, N.A. Danilov, A.A. Murashkin, *High-temperature behaviour of calcium substituted layered neodymium nickelates*, *Journal of Alloys and Compounds* 801 (2019) 558-567
- [15] O. Yamamoto, *Low temperature electrolytes and catalysts from Handbook of Fuel Cells*, John Wiley and Sons, 2010

SYNTHESIS AND CHARACTERISATION OF LITHIUM CERATE CERAMICS FOR BREEDER APPLICATION

Nida Khan^a, Amit Sinha^{a,b*}, S. R. Nair^b, R.K. Lenka^b and V. Sudarsan^{a,c}

^aHomi Bhabha National Institute, Anushakti Nagar, Mumbai, India.

^bPowder Metallurgy Division, Materials Group, Bhabha Atomic Research Centre, Navi Mumbai, India.

^cChemistry Division, Bhabha Atomic Research Centre, Vashi Complex, Navi Mumbai, India.

Abstract: Lithium-based ceramics are considered as promising tritium breeding materials for the test blanket module. High lithium density, good thermal conductivity, low tritium release and thermal and chemical stability are some requirements of ceramic breeder materials. Cerium is most abundant rare earth element on earth. Due to its low neutron capture cross section it is widely used in radiation hardening agent in glass industry and as diluent in nuclear fuels. In $\text{Li}_2\text{O}-\text{CeO}_2$ system, three compounds are known LiCeO_2 , Li_2CeO_3 and Li_8CeO_6 . Lithium cerate has high Li/Ce ratio and high electrical conductivity^[3] which makes it a potential breeder material. To our knowledge, till date no attempt has been made on these compounds for breeder applications. In this investigation, Li_2CeO_3 ceramic was synthesized through solid state reaction and through solution combustion synthesis. The phase purity and structure of calcined powder was confirmed through X-ray diffraction (XRD) and FTIR spectroscopy. Sintering studies were also carried out to get optimised density and grain size requirement for breeder application. The microstructure of the sintered specimens was characterised through scanning electron microscopy and chemical composition was confirmed by ICP-OES.

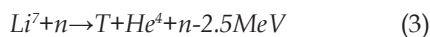
1. Introduction

Fusion energy is believed to be the most prominent energy source in the future. Two isotopes of hydrogen, namely deuterium and tritium are identified as fuels for fusion reaction owing to their high cross-section with least energy requirement^[1]. Deuterium and tritium will fuse in plasma and yield 17.6 MeV of energy according to reaction in equation 1.



For reaction to occur continuously in reactor both fuels have to be supplied uninterruptedly. Deuterium is available naturally in large quantities but tritium due to its small half-life is not abundant in nature, thus it has to be synthesised. Lithium is considered to be most suitable tritium producing element when irradiated with neutrons. It has two isotopes

Li^7 (natural abundance ratio of 92.5 %) which has reaction threshold of ~ 2.5 MeV and Li^6 (natural abundance ratio of 7.5 %) which has higher cross section towards lower neutron energy. Tritium is bred from lithium as per following reactions.



In fusion reactor, blanket surrounds the reactor core and convert neutron energy to heat and also simultaneously breed tritium as shown in fig. 1. Principal functions of blanket in the fusion reactor are:

1. Breed tritium
2. Convert nuclear energy in to heat
3. Neutron shielding

SYNTHESIS AND CHARACTERISATION OF LITHIUM CERATE CERAMICS FOR BREEDER APPLICATION

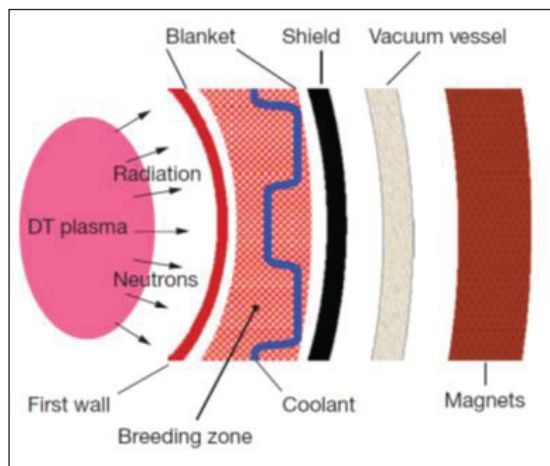


Fig. 1: Schematic of tritium breeding blanket [2]

To satisfy all these functions many materials have been considered which are basically classified in two groups, liquid metal and solid ceramic breeder. Tritium breeding ratio (TBR) is defined as number of tritium atoms produced per incident neutron. $TBR > 1$ is required for compensating losses of tritium in the reactor. To maintain this ratio greater than one, neutron multipliers are added in the blanket system such as Be, Pb. In ITER, various test blanket modules (TBM) with different breeder, multiplier and corresponding coolant combination will be tested. TBM are classified in two breeder blanket concepts; 1) He/Water cooled ceramics blankets and 2) liquid metal (Pb-Li or Li) as a tritium breeder, and helium, liquid metal or a combination of the two as a coolant^[3]. Temperature range of breeder in liquid metal cooled blanket is lower than helium cooled blanket. India has opted for lead lithium cooled ceramic breeder in which breeding zone consist of lithium ceramic pebbles and Pb-Li eutectic flowing between the pebbles to remove heat generated due to neutronic reactions. Tritium is bred both by pebbles and liquid metal. Extraction of tritium is done by purge gas (hydrogen in helium) in ceramic pebbles while external extraction system is there

for liquid metal. Maximum breeder temperature as per this blanket configuration does not exceed 500°C ^[3,4]. Many lithium ceramics have been researched such as Li_2TiO_3 , Li_4SiO_4 , Li_2ZrO_3 , Li_2O but to our knowledge, till date no attempt has been made on lithium cerate ceramics for breeder applications.

In $\text{Li}_2\text{O}-\text{CeO}_2$ system, three compounds are known LiCeO_2 , Li_2CeO_3 and Li_8CeO_6 , Li_2CeO_3 ceramics have already been studied for applications such as lithium-ion batteries, microwave dielectrics, luminescent solar concentrators, radiation hardening agent and as diluent in nuclear fuels^[5,6,7,8]. For the first time we are trying to investigate its properties for breeder applications in nuclear fusion reactor.

2. Experimental

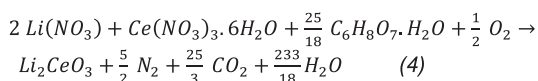
In present study, Li_2CeO_3 ceramic was prepared using both conventional solid state reaction method as well as utilizing the concept of wet chemical synthesis (combustion synthesis) using citric acid as fuel. In the conventional solid state reaction method, Li_2CeO_3 powder was synthesized using dried high-purity lithium carbonate (Li_2CO_3) and cerium oxide (CeO_2) as starting materials. Stoichiometric proportions of raw materials (1:1) were wet-ball milled in ethanol medium using ZrO_2 balls for 24 hours. The mixed powders were dried in an oven and the thermal decomposition behaviour of the dried mixture was analysed by simultaneous thermogravimetric and differential thermal analysis (TG/DTA) under flowing argon at the heating rate of 10 K/min (SETARAM Setsys Evolution 1600). The dried mixture was calcined at different temperature in the range of $500 - 700^{\circ}\text{C}$ for 2 h in air. The calcined powder was uniaxially pressed into compacts with 10-14 mm diameter and 2-5 mm height under the pressure of 150 MPa. The green compacts were sintered between 600°C and 700°C for 2-8 h to achieve the desired density. The phase purity of calcined

SYNTHESIS AND CHARACTERISATION OF LITHIUM CERATE CERAMICS FOR BREEDER APPLICATION

powder and the sintered specimens were identified by X-ray powder diffraction (XRD, INEL). The XRD data were recorded with Cu K α radiation in the 2 θ range of 20° to 80° and the lattice parameters of the formed phase present were determined through Rietveld refinement approach.

Synthesis of Li₂CeO₃ powder through combustion synthesis route

Cerium nitrate [Ce(NO₃)₃·6H₂O], lithium nitrate (LiNO₃) and citric acid (C₆H₈O₇·H₂O) were mixed in the required molar ratios in a minimum volume of de-ionized water to obtain transparent aqueous solutions. The molar ratio of citric acid to metal nitrates was maintained as 1:1. Total oxidising valency of Ce(NO₃)₃ sums out to be 15-, while Li(NO₃) is 5- whereas reducing valency of C₆H₈O₇·H₂O is 18+. Hence, in order to achieve stoichiometric combustion reaction, 1 mol of cerium nitrate needs 15/18 mol of citric acid; similarly, lithium nitrate needs 5/18 mol of citric acid. Using these molar ratios, the redox reaction is expressed in equation 4. This solution was kept on hot plate (~300 °C). After thermal dehydration of the solution the viscous liquid auto ignited with yellow flame releasing large volume of gases and producing dull white powder. The powder thus obtained had carbonaceous content left which was further removed by calcining it to 500 °C for 2 hours.



The chemical compositions of calcined powder and sintered specimen were estimated using inductively coupled plasma atomic emission spectroscopy (ICP-AES, Horiba Yuvon, Ultima 2) by dissolving a representative sample in concentrated mixed acid (HF, HNO₃ and HCl) and subsequent heating on hot plate. Structural information on the calcined powder and sintered specimen was determined with the help of Fourier transformed infrared spectroscopy (FTIR) (Shimadzu, IR affinity 1S). The density of the sintered specimens was evaluated using

Archimedes' principle. The average particle size of lithium cerate powder was measured through laser diffraction particle size analyser (Malvern Zetasizer). The micro-structural characterisation of sintered specimens was carried out by scanning electron microscopy (Zeiss EVO-18) coupled with energy dispersive X-ray analyser (EDS).

3. Results and discussion

Figure 2 shows the TG/DTA curve of the Li₂CO₃ and CeO₂ ball mixed together for 24 hours, up to 1200 °C. The TG/DTA curve so obtained is similar to that of pure lithium carbonate curve. It has been reported that decomposition of Li₂CO₃ is complex process involving melting of Li₂CO₃, dissolution of Li₂O and CO₂, adsorption of CO₂ in Li₂O. Also due to very high melting temperature of Li₂O it is in solid state at lower temperatures which impedes the release of CO₂ [9]. There is a slight weight increment initially which can be attributed as background noise as analysis was done under flowing argon. First DTA peak at ~728 °C corresponds to decomposition of Li₂CO₃ and the second peak (~1035°C) corresponds to melting temperature of Li₂CeO₃. Total mass loss in TG is ~ 13.5% whereas theoretical mass loss calculated as per reaction in equation (5) is 17.89%.

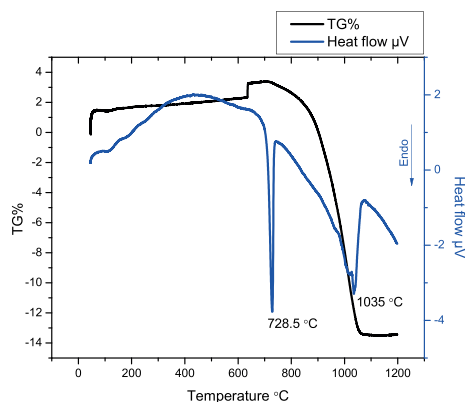


Fig. 2 TG/DTA analysis of Li₂CO₃ and CeO₂ ball milled powder

SYNTHESIS AND CHARACTERISATION OF LITHIUM CERATE CERAMICS FOR BREEDER APPLICATION

Figure 3 shows XRD patterns of Li_2CeO_3 calcined at 700°C for 4 hours in air and sintered at 800°C for 2 hours. The pattern of the calcined powder shows the presence of unreacted lithium carbonate whereas in the pattern of sintered specimen, the strongest peaks corresponding to lithium carbonate were insignificant. It may be mentioned that Li_2CO_3 crystallizes in the same fluorite structure of CeO_2 with Fm3m (No. 225) space group [8]. In the XRD patterns all peaks corresponding to JCPDS file for CeO_2 (#81-0792) were present.

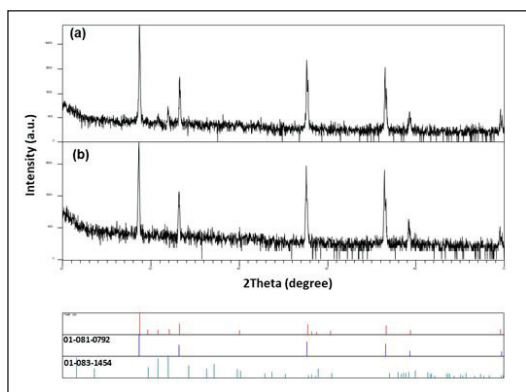


Fig. 3 : XRD Pattern of Li_2CeO_3 powder produced through solid state reaction (a) calcined at 700°C for 4 h and subsequently compacted and (b) sintered at 800°C for 2h

Figure 4 shows the FTIR pattern of sintered Li_2CeO_3 sample. For the purpose of comparison FTIR patterns corresponding to CeO_2 and Li_2CO_3 is also shown in the same figure. The phase, Li_2CeO_3 is characterised by a broad peak asymmetric around 488 cm^{-1} and is attributed to the Ce-O vibration of characteristic of Li_2CeO_3 phase [7]. A comparison of this spectrum with that of CeO_2 and Li_2CO_3 confirms that the Ce-O bond undergo significant change in terms of peak position and line shape when CeO_2 get converted to Li_2CeO_3 . Further, the intense peak around 1500 cm^{-1} in Li_2CeO_3 sample corresponds unreacted Li_2CO_3 present in the samples. Based on the above results it is inferred that, Li^+ ions

in Li_2CeO_3 are occupying interstitial position in CeO_2 . Table 1 shows the composition of the calcined and sintered samples measured through ICP-OES.

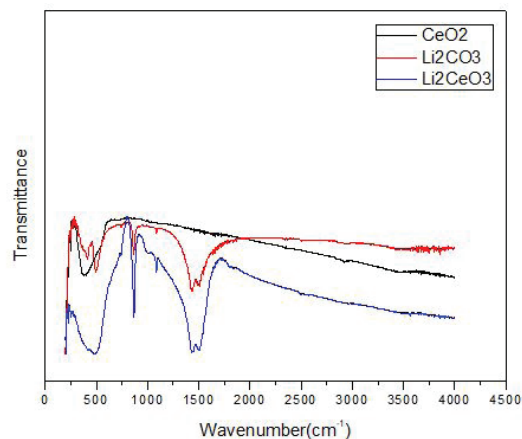


Fig. 4: FTIR spectra of CeO_2 , Li_2CO_3 and Li_2CeO_3

Table 1 Chemical composition of Lithium cerate

Sample	Li (wt%)	Ce (wt%)
Li_2CeO_3 (calcined)	5.2	50.1
Li_2CeO_3 (Sintered)	5.1	50.3

Figure 5 and 6 shows SEM photomicrographs of Li_2CeO_3 heat treated at 700 and 750°C for 3 h in air respectively. The presence of unreacted lithium carbonate can be observed in figure 5, which is minimum in the sample processed at higher temperatures [figure 6].

Since, powder produced through solid state synthesis results in unreacted lithium carbonate, Li_2CeO_3 powder was synthesised using combustion synthesis. The precursor powder was calcined at 500°C for 2 h. The XRD pattern of calcined Li_2CeO_3 powder produced through combustion synthesis route is shown in figure 7.

SYNTHESIS AND CHARACTERISATION OF LITHIUM CERATE CERAMICS FOR BREEDER APPLICATION

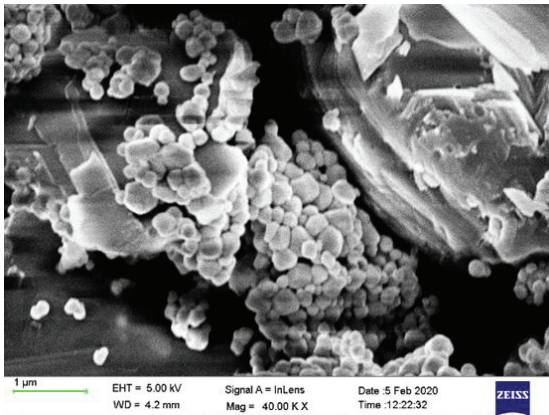


Fig. 5: SEM photomicrograph of Li_2CeO_3 powder produced through solid state reaction of lithium carbonate and ceria powder and calcined at 700°C for 2 h.

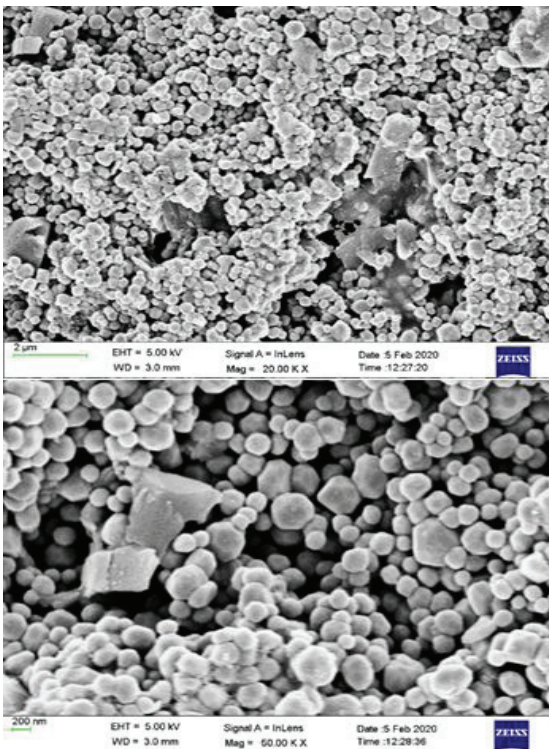


Fig. 6: SEM photomicrographs of Li_2CeO_3 specimen produced through solid state reaction of lithium carbonate and ceria powder and sintered at 750°C for 4 h.

The pattern exhibits all the peaks corresponding to CeO_2 . Using the least square technique, the cell parameter of Li_2CeO_3 was calculated. The calculated lattice parameter of fluorite phase is $5.417(5) \text{ \AA}$, which is close to the reported lattice parameter of Li_2CeO_3 phase.

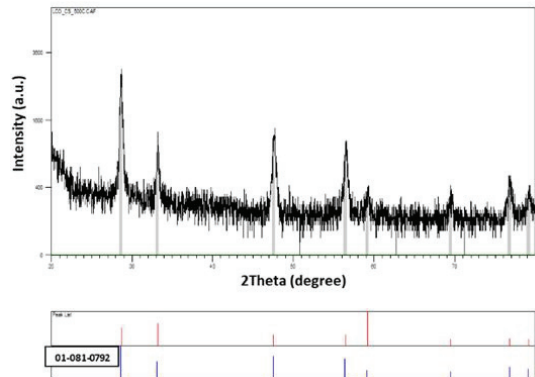


Fig. 7: XRD pattern of Li_2CeO_3 powder produced through combustion synthesis and calcined at 500°C for 2 h.

Figure 8 shows particle size distribution of Li_2CeO_3 powder produced through combustion synthesis. As can be seen from graph it is a bimodal distribution with two mean values of 100 nm and 500 nm. This can be attributed to local rise in temperature during combustion synthesis process. Figure 9 shows SEM images

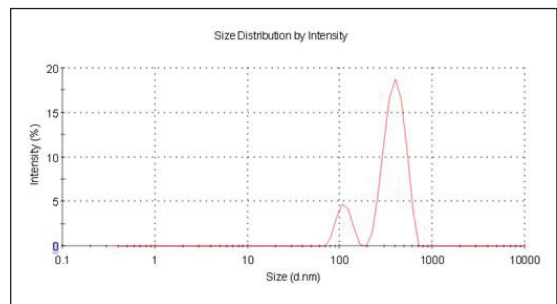


Fig. 8: Particle size distribution of Li_2CeO_3 powder produced through combustion synthesis and calcined at 500°C for 2 h.

SYNTHESIS AND CHARACTERISATION OF LITHIUM CERATE CERAMICS FOR BREEDER APPLICATION

of Li_2CeO_3 pellets sintered at 800°C at different magnifications. Dense and homogenous structure has formed and grain size has increased due to high sintering temperatures.

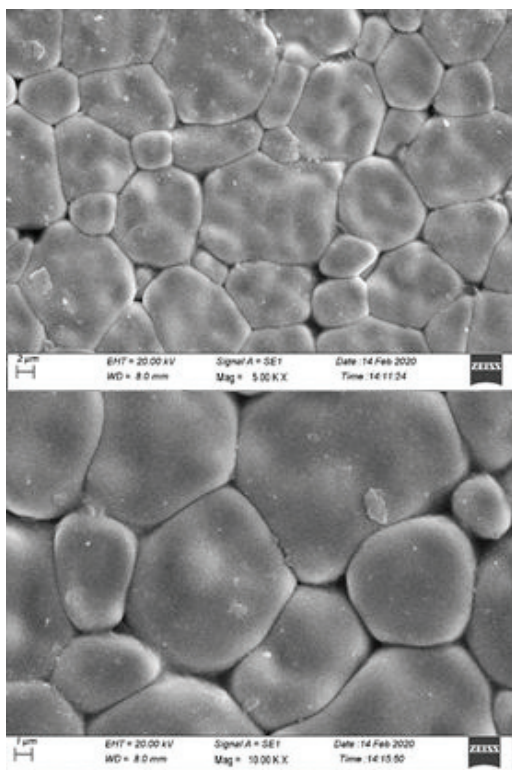


Fig. 9. SEM photomicrographs of Li_2CeO_3 specimen produced through combustion synthesis route and sintered at 800°C for 2 h.

Conclusions

Li_2CeO_3 ceramic was synthesized through solid state route and combustion synthesis route. Pure phase Li_2CeO_3 could not be synthesized through solid state route which had unreacted Li_2CO_3 peak present after calcinations at 700°C . Combustion synthesis yielded fine and pure phase Li_2CeO_3 . Dense and homogenous structure was obtained after sintering at 800°C . Low sintering temperature makes this ceramic promising for breeder application as lithium losses due to volatilisation will be minimised.

References

1. Tanabe, Tetsuo, ed. *Tritium: Fuel of fusion reactors*. Springer Japan, 2017.
2. Johnson, Carl E., K. R. Kummerer, and E. Roth. "Ceramic breeder materials." *Journal of Nuclear Materials* 155 (1988): 188-201.
3. Kirillov, Igor R. "Blanket." In *Fundamentals of Magnetic Thermonuclear Reactor Design*, pp. 291-321. Woodhead Publishing, 2018.
4. Kumar, E. Rajendra, C. Danani, I. Sandeep, Ch Chakrapani, N. Ravi Pragash, V. Chaudhari, C. Rotti, P. M. Raole, J. Alphonsa, and S. P. Deshpande. "Preliminary design of Indian test blanket module for ITER." *Fusion Engineering and Design* 83, no. 7-9 (2008): 1169-1172.
5. Wang, Qiang, Yafei Han, Bingjun Chen, Zhenglin Huang, Shingo Tamaki, Isao Murata, Tieshan Wang, and Kaihong Fang. "Cross sections of (n, x) reactions on cerium isotopes induced by DT neutrons." *Applied Radiation and Isotopes* 147 (2019): 144-151.
6. Tawalare, P. K., V. B. Bhatkar, S. K. Omanwar, and S. V. Moharil. "Broad Band excited NIR emission in Li_2CeO_3 : Nd/Yb phosphor for modification of solar spectrum." *Journal of Alloys and Compounds* 771 (2019): 534-540.
7. Liu, Haowen, Qingwen Liu, and Zhen Yang. "Porous micro/nano Li_2CeO_3 with baseball morphology as anode material for high power lithium ions batteries." *Solid State Ionics* 334 (2019): 82-86.
8. Tseng, Ching Fang, and Po An Lin. "Microwave Dielectric Properties of Novel Glass Free Low Firing Li_2CeO_3 Ceramics." *Journal of the American Ceramic Society* 97, no. 4 (2014): 1020-1022.
9. Timoshevskii, A. N., M. G. Ktalkherman, V. A. Emel'kin, B. A. Pozdnyakov, and A. P. Zamyatin. "High-temperature decomposition of lithium carbonate at atmospheric pressure." *High Temperature* 46, no. 3 (2008): 414-421.